The electric and optical properties of doped small molecular organic light-emitting devices

by

Kwang-Ohk Cheon

A dissertation submitted to the graduate faculty

in partial fulfillment of the requirements for the degree of

DOCTOR OF PHILOSOPHY

Major: Condensed Matter Physics

Program of Study Committee:
Joseph Shinar, Major Professor
John R. Clem
Alan I. Goldman
David Carter-Lewis
Gary Tuttle

Iowa State University

Ames, Iowa

2003

Graduate College
Iowa State University

This is to certify that the doctoral dissertation of

Kwang-Ohk Cheon

has met the dissertation requirements of Iowa State University

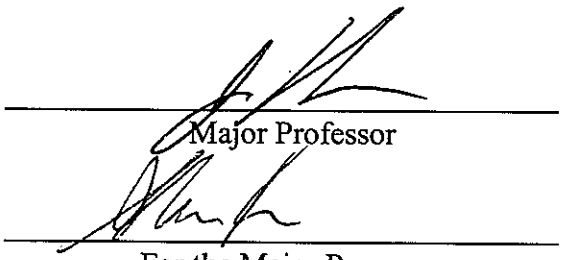

Major Professor

For the Major Program

TABLE OF CONTENTS

1. GENERAL INTRODUCTION

What is an organic light-emitting device (OLED)?

Organic light-emitting devices (OLEDs) constitute a new and exciting emissive display technology. In general, the basic OLED structure consists of a stack of fluorescent organic layers sandwiched between a transparent conducting-anode and metallic cathode [1,2]. When an appropriate bias is applied to the device, holes are injected from the anode and electrons from the cathode; some of the recombination events between the holes and electrons result in electroluminescence (EL). Until now, most of the efforts in developing OLEDs have focused on display applications, hence on devices with in the visible range. However some organic devices have been developed for ultraviolet [3] or infrared [4] emission.

History of organic electroluminescence

Organic EL from anthracene crystals was observed by M. Pope *et al.* [5] and W. Helfrich *et al.* [6] in the early 1960s. To detect it, very high voltage was needed due to thickness of the anthracene crystals (10 μm ~ 5 mm); the operating voltage ranged from several hundred to several thousand volts. Due to these requirements, EL from anthracene and related crystals has long been of interest to basic research in optical characteristics and electrical transport mechanism rather than commercial applications. Indeed, although in 1982 P. S. Vincett *et al.* [7] achieved bright blue EL from vacuum-deposited 0.6 μm thick anthracene

crystal films with an applied bias of less than 100 V, this voltage was still not appropriate for display purposes.

Dramatic progress was achieved in 1987 by C. W. Tang and S. A. VanSlyke [1], who fabricated 100 nm thin bilayer devices. The devices were made of evaporated small molecular weight organic materials including N, N'-diphenyl-N, N'-bis(3-methylphenyl) 1-1'biphenyl- 4,4' diamine (TPD) and tris(8-hydroxyquinoline) aluminum (Alq_3). They achieved a very high brightness of more than 1000 Cd/m^2 and a high external quantum efficiency of 1 % (photons/electrons) at an applied bias of less than 10 V. The thin organic structure (overall thickness ~ 100 nm) reduced the operating voltage to a manageable range for displays, and the bilayer structure increased the luminous efficiency. Following this achievement, Adachi *et al.* [8] succeeded in fabricating the stable multi-layer devices by inserting hole, emitting, and electron transport layers between the two electrodes. In 1989, Tang *et al.* [2] developed a laser-dye doped Alq_3 multilayer structure, in which the fluorescent efficiency was improved, and the emission color varied from the original green color of Alq_3 to the dopant emission color.

Another dramatic achievement in organic EL was the discovery of polymer EL in 1990 by J. H. Burroughes *et al.* [9]. Compared to small molecular devices, polymer light-emitting devices (PLEDs) have several potential advantages, *e.g.*, fabrication by spin-coating [9,10] or inkjet-printing [11] from solutions, and subsequent thermal treatments.

In general small molecule and polymer OLEDs make use of the fluorescent emission of singlet excitons. If the injected hole and electron carriers recombine randomly, then the probability of forming spin-singlet and spin-triplet states is 25 % and 75 %, respectively. The ideal maximum fluorescent yield is therefore limited to 25 % by spin statistics. To

overcome this theoretical limit, M. A. Baldo *et al.* [12] suggested and demonstrated phosphorescent OLEDs, where the EL is due to triplet emission, by doping phosphorescent molecules into a fluorescent host layer. Thus, the theoretical limit of molecular EL efficiency was increased from 25 % to 100 %. Recently, P. W. Wang *et al.* [13] and J. N. G. Pillow *et al.* [14] have developed macromolecular EL devices, based on dendrimers. The dendrimers are composed of a luminescent core and branching dendrons that protect the exciton on the core. However, the transport properties of dendrimer films worsen with increased branching or dendrimer generation [15].

Advantages and disadvantages of OLEDs

OLEDs are already commercialized, and making inroads into liquid crystal display (LCD) markets. Currently, most of the commercialized OLEDs are used in low information displays with limited size such as mobile phones, PDAs, digital cameras, and some palmtop computers. They have several driving and technological advantages over LCDs.

Advantages:

- **Self-luminous**. Backlighting, diffusers, and polarizers are not needed, so the overall efficiency is better than that of LCDs.
- **Low cost and easy fabrication**. Roll-to-roll manufacturing processes (such as inkjet printing and screen printing) are possible for polymer LEDs.
- **Color selectivity**. A variety of organic materials have been developed for blue to red emission.
- **Lightweight, compact, and thin devices**. The total thickness of the organic layers is only about 100 nm.

- **Flexibility.** It is easy to fabricate OLEDs on flexible plastic or on curved substrates.
- **High brightness and high resolution.**
- **Large emissive displays.**
- **Wide viewing angle** (up to 160 degrees).
- **Fast response** (decay time < 1 μs).

The disadvantages of OLEDs are mainly related to their lifetime. The organic materials are sensitive to oxygen and moisture, so encapsulation is required to protect the devices from degradation agents. With proper encapsulation, lifetime exceeding 10,000 hours have been demonstrated [16].

Disadvantages:

- Relatively short lifetime due to sensitivity to air and moisture.
- Low glass transition temperature T_g for small molecular devices (> 70°C). The operating temperature cannot be beyond T_g.
- Low mobility requiring high applied bias. To inject and transport charge carriers in dispersive organic media, very high electric fields (0.1 – 2 MV/cm) are needed.

Basic OLED structure

Small molecular OLEDs are typically fabricated on glass or flexible plastic substrates coated with a transparent conducting anode such as nonstoichiometric indium tin oxide (ITO). The organic layers are thermally evaporated on the anode substrate with a total thickness of about 100 nm, and then a low work function metal cathode is deposited on the organic layers (Fig. 1). If a forward bias is applied to this structure, holes (h^+'s) are injected

from the anode, and electrons (e^-'s) from the cathode. The injected carriers recombine, form excitons, and some of these decay radiatively. Normal operating voltage is about 2 - 20 V, corresponding to average electric fields of 0.1 - 2 MV/cm, which are very high compared to the typical fields ~ 10 kV/cm in inorganic semiconductor devices. The resistivity ρ of the devices ranges over more than eight orders of magnitude, with very high values of $10^5 - 10^{13}$ Ω·cm in forward bias. In reverse bias, ρ is also very high (10^9 Ω·cm). Therefore, the OLEDs generally exhibit poor rectifying properties.

ITO is generally a wide band gap amorphous semiconductor (E_g = 3.5 - 4.3 eV) [17]; the material is composed of indium oxide (In_2O_3) and a small amount of tin oxide (SnO_2) (~ 5 wt%). Most OLEDs use ITO as the anode due to its relatively high work function and its unique transparent-conducting characteristics. The conductance and transparency of ITO are mostly dependent on the film thickness and the composition ratio of the two components. The resistivity of 200 nm thick ITO the resistivity is about $\rho \sim 10^{-3}$ Ω·cm with mobility $\mu \sim$ 10 cm^2/Vs [17]. With increased ITO thickness the conductance increases, but the transparency decreases. The ITO transparency is normally quite high in the visible range; typical transmission is more than 90 % for 150 nm thick ITO [17]. Another very important ITO parameter is its work function (ϕ_b) or Fermi energy (E_f) relative to the organic materials. Because the highest occupied molecular orbital level (HOMO) energies of organic materials are typically E_{HOMO} = 5 - 6 eV, a ϕ_b is needed for the anode to enable efficient hole injection into the organic layer.

The work function ϕ_b of ITO varies widely according to its surface treatment (ϕ_b = 4.1 – 5.1 eV) [18-20]. The mechanisms of ϕ_b variation caused by surface treatments have been

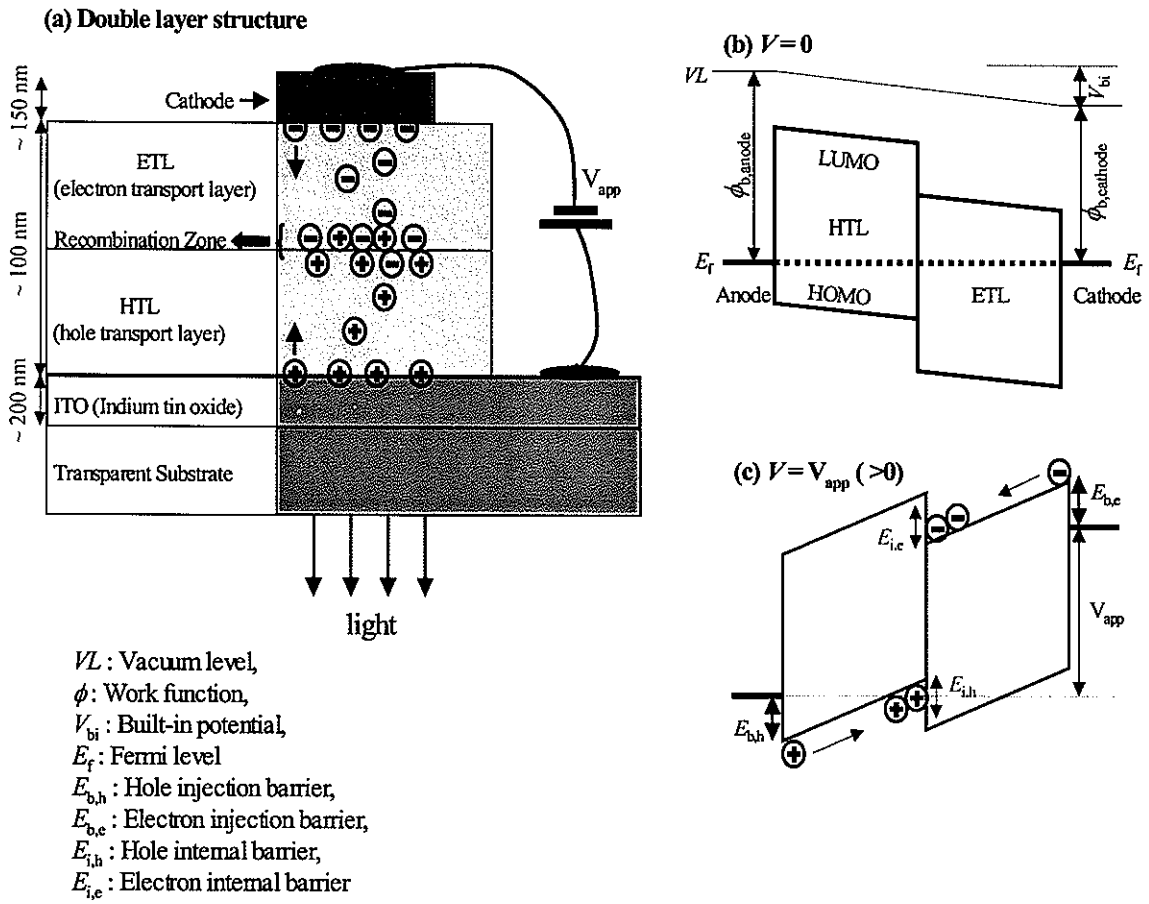

Figure 1 Double layer device structure (a), equilibrium state energy levels at applied bias $V = 0$ (b), and energy levels at a forward applied bias $V = V_{app}$ (c).

studied extensively and are still disputed. Ultraviolet photoelectron spectroscopy (UPS) and x-ray photoelectron spectroscopy (XPS) studies [19-23] have shown that ϕ_b could be changed by a generated dipole layer and/or a modified electronic structure of ITO caused by surface treatments. The surface dipole layer changes the vacuum level of the ITO/organic interface [21] to reduce the energy barrier for hole injection.

For the cathode, low work function materials such as Ca ($\phi_b \sim 3$ eV), Mg ($\phi_b \sim 3.7$ eV), and/or Al ($\phi_b \sim 4.3$ eV) [24] are used to minimize the energy barrier for e^- injection from E_f of the cathode to the lowest unoccupied molecular orbital (LUMO) level of organic materials (typical $E_{LUMO} = 2 - 3$ eV). The problem of many low work function metals is extreme reactivity to oxygen and water, so Ca and Mg should be protected by an additional layer such as Al. Another way to minimize the barrier for electron injection is to insert a very thin (~ 1 nm) insulating layer of LiF, CsF, or AlO_x [25] between the top organic layer and the Al cathode; in general LiF and CsF are more effective than AlO_x. These buffer layers apparently generate a dipole layer, and thus reduce the barrier for electron injection like the dipole layer on the ITO by surface treatments. A photoelectron spectroscopy study [26] has shown that CsF is decomposed by Al metal deposition; the F atoms react with Al to form AlF_3. The dissociation likely results in Cs^+ and *n*-doping of the organic layer at the interface: Consequently, a dipole layer is generated between the Cs^+ and *n*-doped organic layer, which probably improves electron injection from the Al cathode.

Energy level alignment is shown at Fig. 1(b) at an applied bias $V_{app} = 0$ V. In the equilibrium state at 0 V, the vacuum levels (*VL*s) of the anode and cathode are shifted relative to each other to align the Fermi energies at the same level. The energy (or potential) needed to make flat-band state is called the built-in potential (V_{bi}). It is determined by the *VL*

shift at $V_{app} = 0$ V. Typical values of V_{bi} are 1.5 – 3 V, similar to the energy gap of the organic material in the case of ohmic contact.

The hole and electron transport layers (HTL and ETL, respectively) are the layers favorable for hole and electron, respectively. When $V_{app} < V_{bi}$, the injected current is negligible, and the most of current is caused by free carriers in the organic layers or leakage current. Hence it is proportional to the low applied voltage V_{app} (ohmic dependence). With increasing forward bias, more charges are injected from electrodes. At high applied field the injected holes and electrons hop from site to site through the organic layers. Some of the carriers may accumulate in a specific area, called charge accumulation zone, usually at the organic-organic interface of multi-layer structures. If the density of holes and electrons is sufficiently high, then the distance between them becomes sufficiently low for recombination to radiative singlet excitons (SEs).

The reasons for fabricating multilayer OLEDs are to improve the balance between e^- and h^+ injection and to confine the charge accumulation zone to a specific region away from the electrodes, since the electrodes quench the SEs [27]. If we choose proper materials for the HTL and ETL, then the charges accumulate at the HTL/ETL interface, i.e., relative far from the electrodes.

In general the HTL/ETL interface presents significant energy barriers and mobility offsets for both holes and electrons. The holes injected from the anode drift quickly to the interface, but due to a high hole barrier they accumulate on the HTL side of the interface (Fig. 1(C)). Similarly, electrons accumulate on the ETL side of the interface. The energy barriers and mobility offsets at the organic-organic interface are not always symmetric, so the hopping probabilities of either holes or electrons from their layer to the next other layer may

be different. Typically, the hole hopping probability is greater than the electron hopping probability, especially in the common multilayer devices [N,N'-diphenyl-N,N'-bis(1-naphthylphenyl)-1,1'-biphenyl-4,4'-diamine (α-NPD)]/Alq_3 and α-NPD/[4,4'-bis(2,2'-diphenyl-vinyl)-1,1'-biphenyl (DPVBi)]. That is why in these OLEDs, most of the emission is due to the ETL, i.e., Alq_3 and DPVBi.

Carrier transport in organic devices

Organic solid and traps

The transport mechanisms in organic solids are not fully understood. The difficulties and complications of the transport processes are due mainly to the trap states in these organic materials. Without comprehensive knowledge of the distribution and characteristics of these traps, it is not possible to understanding the exact current-voltage properties of OLEDs.

Basically, there are two types of traps, intrinsic and extrinsic [28]. Intrinsic traps are due mostly to the amorphous structure of the organic film. They include conformational defects, grain boundary defects, and molecular structural defects. Even in the perfect molecular crystal, the carrier can be localized in a specific molecule due to the molecular crystal characteristics of relative weak interaction between molecules.

Extrinsic traps are typically generated by chemical impurities, somehow unavoidable due to the nature of the synthesis or device fabrication processes, or by intentional doping. These traps and the localized states they generate are closely related to the transport mechanisms and EL properties of OLEDs. Almost all organic devices show trap-related transport behavior.

(a) Crystalline molecular solids

Before discussing the localized states in crystalline molecular solids, remarks on the difference between molecular and inorganic crystals may help clarify not only some of the transport properties but also some of the electro-optic characteristics of OLEDs. Inorganic semiconductors are composed of regular arrays of unit cells, in which continuous conduction and valence bands are generated. Thus the electrons in the conduction bands are free to move without passing through any localized state. The carrier transport is then described by a band structure mechanism. In particular, the carrier mobility is independent of the electric field. In case of excited states, the excitons of inorganic semiconductors are very loosely bound Mott-Wannier excitons, with binding energies ~ 10 meV [29], i.e., smaller than room temperature thermal energy.

In contrast to inorganic crystals, molecular crystals are made of discrete molecules generally held together by van der Waals forces [30]; the molecule itself consists of atoms bounded to each other by strong covalent bonds. The van der Waals interaction between neighbor molecules is relatively weak compared to the strong interaction between the unit cells in inorganic crystals.

Figure 2 shows the electronic structure of a linear molecular crystal. The most peculiar feature of the structure is the spatial localization of the valence and conduction bands with narrow band-widths (< 0.1 eV) [31]. Due to the localization, these levels are labeled as highest occupied molecular orbital (HOMO) and lowest unoccupied molecular orbital (LUMO), rather than valence and conduction bands. The transport properties of carriers are affected by the localization of the HOMO and LUMO states, as the localized carriers move from site to site either by thermal- or electric field-assisted hopping. Hence typical

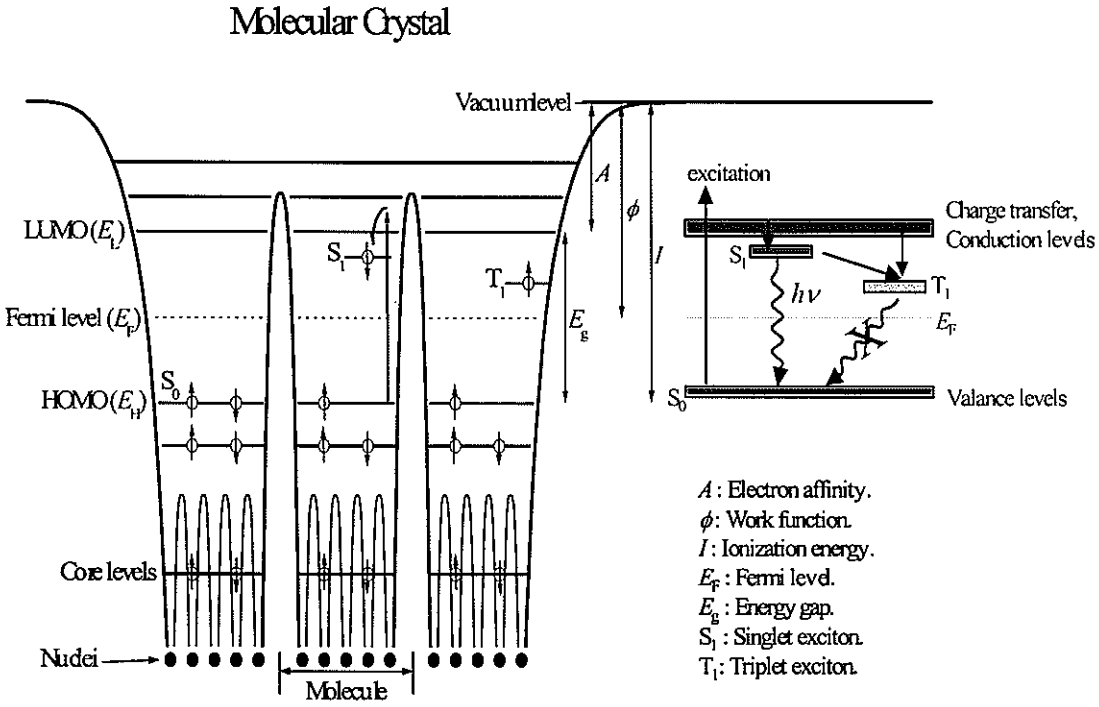

Figure 2. Electronic structure of an organic molecular solid.

mobilities in molecular crystal are only ~ 1 cm^2/Vs [32]. The mobility may be calculated using either a hopping or band mechanism, depending on the degree of localization. If localization is strong, then the mobility is explained by a hopping model; if it is weak, then it exhibits band-like characteristics [33].

The excited states of a molecular crystal can be generated by absorbing an incident photon (photogeneration) or by the recombination of electrically injected holes and electrons. The excited state can relax internally to a lower vibrational and/or electronic manifold without changing spin state. Normally, this internal relaxation is fast, and thus virtually all of the luminescence emitted by the molecules occurs from the lowest excited singlet state (S1 in Fig. 2). Fluorescence is emitted as a result of the radiative decay from the lowest excited state in the singlet manifold (S1) to the ground state (S0).

The binding energy of the S1 singlet exciton state is generally quite high (typically 0.1 eV) compared to the excitons in inorganic semiconductors. These strongly bound excitons are called Frenkel excitons.

In addition to the fluorescence decay of S1, there is a certain probability for a conversion from S1 to the lowest excited triplet state (T1). Since this process involves a change of spin multiplicity, it is called intersystem crossing (ISC). The decay from T1 to S0 state is generally forbidden by the selection rules. However, certain second order effects may weakly allow the decay, and the emission resulting from this decay process is known as phosphorescence.

(b) Amorphous molecular solids

Small molecular OLEDs are generally fabricated by vacuum evaporation of the small molecules. The amorphous structure resulting from this deposition process generates a broad distribution of the molecular orbital levels (~ 0.1 eV) and traps. The transport properties are affected drastically by the trap states. However, the luminescence of the device is not significantly affected by the traps, because the emission is due to the strongly bound Frenkel excitons. The trap densities are typically ~ 10^{18} cm^{-3} for a vacuum evaporated Alq_3 [34], corresponding to ~ 1 mol.%. The distribution of trap energies is typically exponential, rather than single discrete trap energy levels. This exponential trap distribution is easy to analyze mathematically, compared to a Gaussian trap distribution.

The exponential distribution of trap energies is represented by a characteristic energy E_t and the number of traps N_0 per unit energy at the HOMO and LUMO levels; typically, E_t ~ 0.15 eV and N_0 ~ 10^{18} cm^{-3} in both small molecular [34] and polymeric amorphous films [28]. Under typical operating applied fields, the carrier is typically around 10^{-6} – 10^{-3} cm^2/Vs, and strongly affected by the sample preparation conditions.

(c) Extrinsic impurities

As mentioned above, the traps can also be generated by chemical impurities originating from the chemical synthesis or the device fabrication processes. Normally, these impurities generate very deep carrier trap. When a low voltage is applied, these deep traps are rapidly filled by the carriers [28]. Therefore, the deep traps do not affect the transport properties at higher applied bias.

Finally another very important impurity is intentional doping, *e.g.*, for the fabrication of a guest-host (G-H) system to lower the emission wavelength and/or increase the device efficiency. The molecularly doped G-H system will be discussed later in detail.

Mobility

Carrier transport in disordered molecular solids is strongly dependent on temperature and applied electric field [35]. Due to the disordered structure and localized states the carriers can be trapped very easily. Thus, the transport properties in organic amorphous solid are analyzed by hopping models [36]. In the typical hopping model, the mobility μ is assumed to follow an Arrhenius dependence on the temperature T:

$$\mu = \mu_0 e^{-E_a/kT}, \tag{1}$$

where μ_0 is the trap independent or field-independent mobility, E_a is the activation energy to overcome the local energy barrier, and kT is the thermal energy. As mentioned above, the typical value of E_a is about 0.15 eV for molecular crystals.

(a) Phonon-assisted hopping [30].

If the molecular lattice is disordered, or the carrier becomes localized on a defect site, then lattice vibrations or phonons can improve carrier movement to another site. The lattice vibration modifies the local potential, and at the opportune instant, the carrier can hop easily through the deformed energy barrier (Fig. 3). Hence, to phonon assisted hopping, the mobility depends on T in an Arrhenius manner. Indeed, the behavior of the mobility of oligothiophenes is Arrhenius-type, with activation energy $E_a \sim 0.1$ eV [37].

(b) Electric-field-assisted hopping

In general carrier mobility in inorganic semiconductors is independent of the applied filed, but in disorder organic films the mobility is a function of the field F. If a carrier is trapped in a potential well (the symmetric dotted lines in Fig. 4), then it needs an activation energy E_a to jump out of the well. When field F (the linear line in Fig. 4) is applied, the potential is deformed into the asymmetric curved lines: One side of the potential barrier increases, and the other side decreases. Thus the actual decrease of the potential barrier or activation energy is proportional to $\sqrt{F}$ (see next section). Therefore, Eq. (1) must be modified to reflect the electric field dependence of the mobility. This is described by the Poole-Frenkel relation [30],

$$\mu = \mu_0 e^{\sqrt{F/F_0}}, \tag{2}$$

where F_0 is a temperature dependent coefficient.

The zero-field mobility μ_0 of organic amorphous solids is typically 10^{-9} – 10^{-4} cm^2/Vs at room temperature. In most π-conjugated molecules, the hole mobility μ_{h0} is higher than the electron mobility μ_{e0}; notable exceptions include the ETL materials Alq_3 and DPVBi. In the HTL materials TPD and α-NPD, the time of flight measurements yielded $\mu_{h0} \sim 5\times10^{-4}$ cm^2/Vs, with the field dependent parameter $1/\sqrt{F_0} \sim 10^{-3}(cm/V)^{1/2}$ [38]. However, the e^- minority carrier mobility in these materials was too low to measure. Thus, in many cases the minority carrier mobility is assumed to be ~ 2 orders of magnitude lower than the majority carrier mobility. For the popular ETL material Alq_3, the μ_{e0} was ~ 10^{-9} – 10^{-6} cm^2/Vs with $1/\sqrt{F_0} \sim 10^{-2}$ $(cm/V)^{1/2}$ [39]. These values, however, are very strongly affected by the sample preparation conditions.

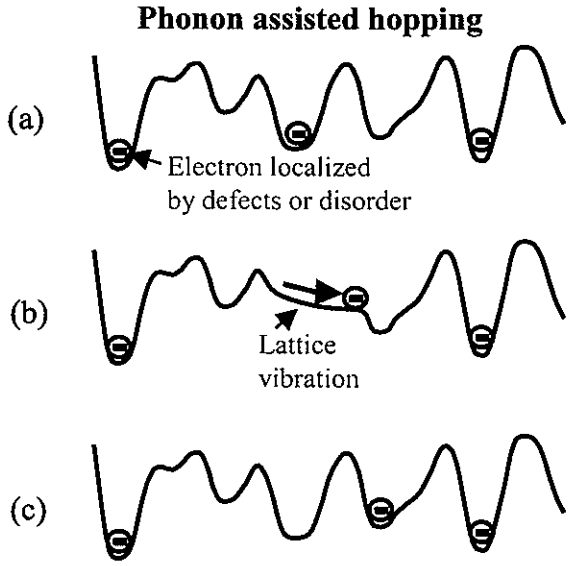

Figure 3. Hopping transport. Due to the lattice vibration a local potential well is distorted, and the trapped electron can move to another site.

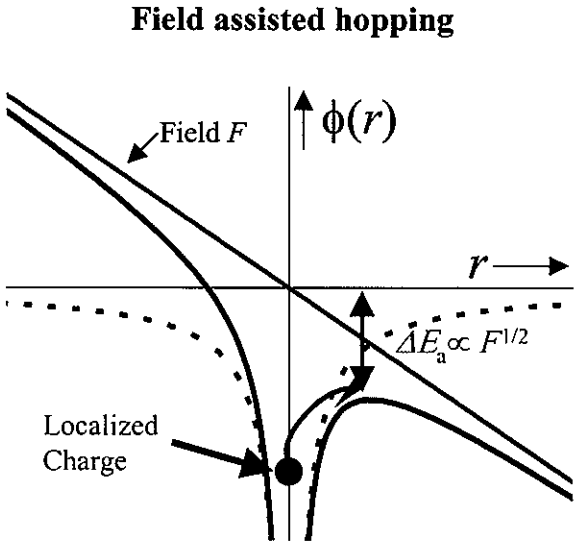

Figure 4. Field assisted hoping. When an electric field F is applied (blue linear line), the symmetric potential well (black dotted-lines) transforms to the asymmetric well (red lines). Hence the field lower the energy barrier and the actual activation energy, increasing the escape probability of a trapped charge.

Injection-limited current

(a) Image force lowering [24]

When carriers are injected from a metal electrode into the organic layer (Fig. 5), they encounter the injection barrier $q\phi_m$, which is the energy difference between the Fermi level E_F of the metal and the LUMO level E_{LUMO} for electron injection. Similarly, holes encounter a barrier, which is the difference between E_F and E_{HOMO}. Following injection, many electrons remain on the surface of the organic layer at distance $+x$ from the metal-organic interface. These electrons induce equivalent hole charges in the metal layer at $-x$. The hole charges are referred to as image charges. The force between the electrons and the induced holes is an attractive force, called the image force, and is given by

$$F_{image} = -\frac{q^2}{16\pi\varepsilon \cdot x^2}, \tag{3}$$

where ε is the permittivity of the organic material (usually $\varepsilon \sim 3\varepsilon_0$, where ε_0 is the free space permittivity). The energy work done by image charge corresponds to the energy barrier between the metal and the organic material $q\phi_m$:

$$q\phi_m = -\frac{q^2}{16\pi\varepsilon \cdot x}. \tag{4}$$

When a field F is applied, the total potential energy is given by the sum of $q\phi_m$ and external field energy qFx. Then the new potential barrier (red lines in Fig.5) of the metal-organic interface system becomes

$$q\phi_B = -\frac{q^2}{16\pi\varepsilon \cdot x} - qFx. \tag{5}$$

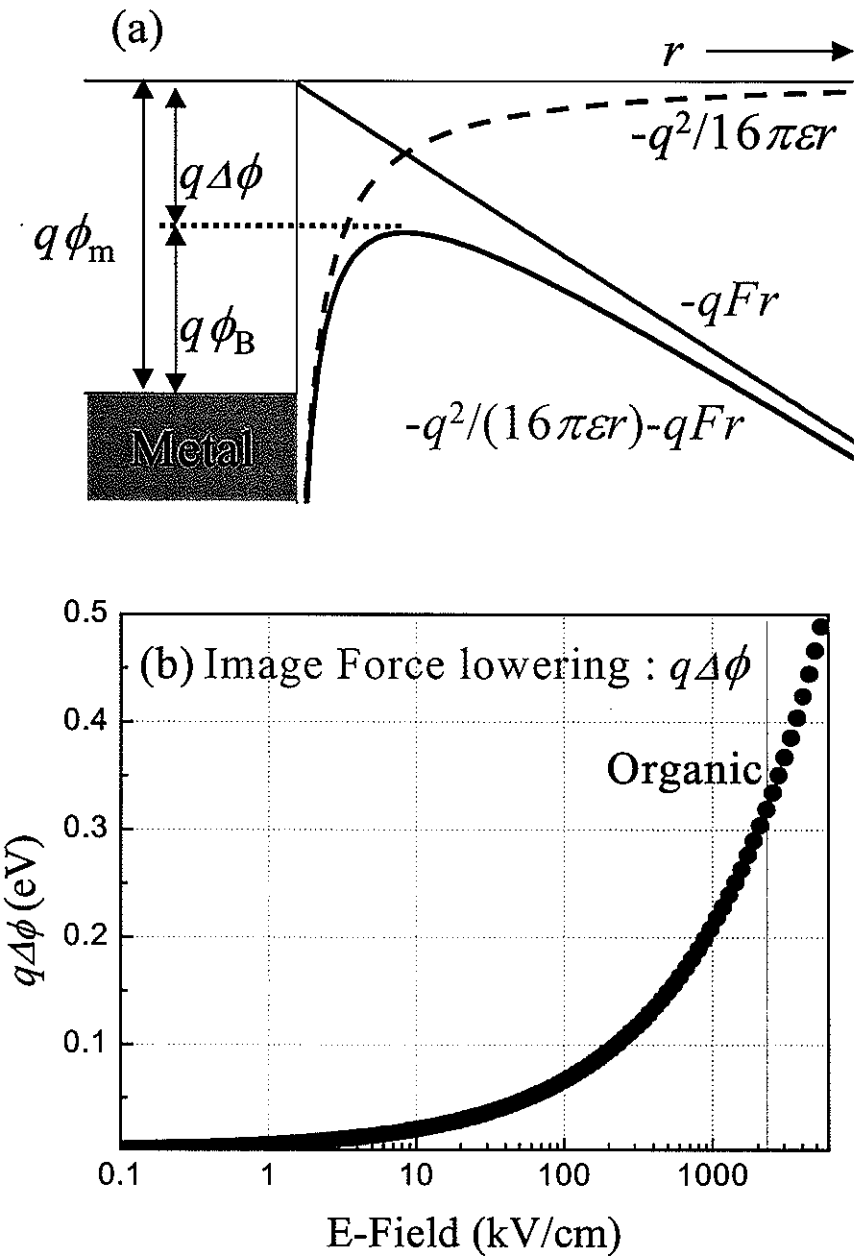

Figure 5. (a) Image force of the barriers for electron injection at the metal-organic interface. The energy barrier at the interface is lowered by an amount $q\Delta\phi$ from $q\phi_m$ to $q\phi_B$. (b) The image force lowering $q\Delta\phi$ *vs.* applied field. The shaded area is the region of typical fields for OLEDs.

The actual potential ϕ_B is lowered as a result of the combination of the image force and field; it is lowered by an energy $\Delta\phi$ given by

$$\Delta\phi = -\sqrt{\frac{qF}{4\pi\varepsilon}}. \tag{6}$$

Unlike the normal inorganic semiconductors, the image force lowering is very important in organic devices due to the high applied field F. Additionally the permittivity of organic materials is relatively small ($\varepsilon_{organic} \sim 3\varepsilon_0$) in comparison to the permittivity of inorganic semiconductors where typically $\varepsilon_{inorganic} > 10\varepsilon_0$. Hence, the image force lowering is more effective in organic than inorganic devices.

Figure 5 (b) shows $q\Delta\phi$ *vs.* average applied field. The $q\Delta\phi$ is about 0.1 – 0.3 eV for typical operating fields of OLEDs. This barrier lowering is very crucial for energy barriers $q\phi_m$ in the range of 0.2 - 1 eV. For instance [40], the Al/Alq_3 interface has a 1.0 eV barrier for electron injection, since the LUMO level is at 3.0 eV, and Al has 4.0 eV work function. Thus, electron injection would be very poor through this high barrier without the image charge lowering [41].

(b) Thermionic injection [24]

The current-voltage characteristics of OLED depend critically on the electronic states at the metal-organic interface. Charge injection at low applied bias is primarily due to thermal emission of charge carriers over the interface potential barrier when the barrier is not too high for thermal injection. The thermionic injection current density (J_{th}) over the barrier

depends on the modified energy barrier ($q\phi_B$), modified by the image force and on the temperature (T). It is given by

$$J_{th} = A^* T^2 e^{-q\phi_B / kT}, \tag{7}$$

with Richardson's constant A^* given by

$$A^* = \frac{4\pi q m^* k^2}{h^3}, \tag{8}$$

where m^* is the carrier effective mass. Due to the field-dependent image-force-lowering of the barrier, J_{th} increases with increasing bias. For free electrons ($m^* = m_e$), the Richardson constant for thermionic emission into the vacuum is 120 Amp/cm^{2}K^2.

If thermal equilibrium prevails, the backflowing interface recombination current cancels out of the thermionic injection current. The evaluation of the interface recombination current is not easy in organic device compared to the well-defined band-type current in inorganic semiconductors. Thus Davids *et al.* [42] described the interface current density (J_{ir}) as

$$J_{ir} = \gamma p(0), \tag{9}$$

where $p(0)$ is hole carrier density at the interface $x = 0$, and γ is determined by detailed balance between thermionic injection and interface recombination, where the latter is independent of bias. At low applied bias the interface recombination current is almost, but slightly less than the thermionic current ($|J_{ir}| \leq |J_{th}|$). Thus, the total current through the device (J_{dev}) is much smaller than the thermal injection current (typically $J_{dev}/J_{th} \propto 10^{-6} - 10^{-3}$), where J_{th} is calculated assuming A^* = 120 Amp/cm^{2}K^2 [42]. However, from temperature-dependent current measurements, A^* is about 3 – 10 orders of magnitude less than A^* for free electrons [43]. The reasons for the low constant and large

deviation from the free electron case are partially due to the ambiguity of the molecular levels, level broadening, and trap states at the interface. For example, in the literature the molecular energy levels of Alq_3 vary considerably. The value of E_{HOMO} ranges from 5.6 to 6.0 eV, and the value of E_{LUMO} varies from 2.7 to 3.2 eV. The LUMO level broadening σ_{LUMO} of Alq_3 is up to 0.35 eV at the metal contact [44].

(c) Field dependent tunneling [43]

Field emission is the process whereby carriers tunnel through a barrier in the presence of a high electric field. When the barrier is triangular, the tunneling is called Fowler-Nordheim. This process is an important mechanism for transport through thin energy barriers. The total thickness of the organic layers in typical OLEDs is about 100 nm. When the forward field is increased, the triangular energy barrier becomes shallower (Fig. 1(c)) [42]. It is typically ~ 2 nm wide at an applied field of 2 MV/cm, in which case the width is sufficiently thin for tunneling. For the triangular barrier, the tunneling probability T_{tu} may be calculated using the WKB approximation. The resulting electric field dependent expression for T_{tu} is [43]

$$T_{tu} \approx e^{-\frac{4\sqrt{2m^*\phi_B^3}}{3q\hbar F}}. \tag{10}$$

Note that this tunneling probability vanishes as $F \to 0$, as expected. In principle, the electron current density is the product of the charge q, carrier velocity v, and electron density n_e,

$$J \equiv dQ/dt = qvn_e \tag{11}$$

where Q is the total charge per unit area. The tunneling current through the triangular barrier is then determined by the average electron velocity v approaching the barrier, the available carrier density n_e, and the tunneling probability as given by Eq. (11). The result is [24]

$$J_{tu} = J_{FN} \approx AF^2 e^{-F_0/F}, \tag{12}$$

with parameters A and F_0 related to the potential barrier and given by

$$A = \frac{mq^3}{8\pi\hbar m^* \phi_B}, \; F_0 = \frac{8\pi\sqrt{2m^*\phi_B^3}}{3qh}. \tag{13}$$

The barrier ϕ_B itself is also a function of F by through the image-force lowering effect. Typically, for low fields (< 2MV/cm), the thermionic current dominates; for high fields (> 2 MV/cm), the tunneling current prevails [42].

Space charge limited current [45]

By high fields, the barrier at the metal/organic interface becomes sufficiently thin and the current is then determined by the bulk properties. Due to the high resistivity of organic materials, the current flow through the bulk, contains traps, is called space-charge-limited-current (SCLC). The total current flowing through an insulator is determined by the drift current, which depends on the electric field, and the diffusion current, which is determined by the concentration gradient. However, at high fields, the diffusion current can be neglected, except at the interface regions. For negligible diffusion current the field will be uniformly distributed over the insulator length L, and will be equal to the average field $F = V/L$.

In trap-free insulators, when the thermally generated electron density n_{e0} dominates the total electron density, μ is independent of field and therefore the drift current density J_{ohmic} (Eq. (11)) follows Ohm's law,

$$J_{ohmic} = qn_{e0}\mu\frac{V}{L}. \tag{14}$$

However, in a typical organic semiconductor, $n_{e0} \leq 10^{10}$ cm^{-3}. Normally in organic solid, the free carrier density n_{e0} is small and about less than 10^{10} cm^{-3}. In addition, traps are almost always present. Their presence results in a greatly reduced current at low bias, because these traps, which are initially empty, capture most of the injected carriers. Note that if an electron trap level E_t lies above Fermi level E_f, but $E_t - E_f > kT$, then the trap is considered as shallow; if $E_t - E_f < kT$, then it is considered as deep.

In accounting for the role of the traps, we first express the total electron concentration as the sum of the concentration in the shallow traps n_t and free electrons n_e:

$$n_{tot} = n_t + n_e. \tag{15}$$

If $n_t >> n_e$, then the total number of trapped charges per unit area Q is

$$Q \approx n_t L \approx \left(\frac{CV}{L}\right)L \approx \frac{\varepsilon V}{L}, \tag{16}$$

where L is the organic layer thickness and C is the capacitance per unit area. Combining Eq. (16) and (11), the current density J_{SCLC} for the shallow trap case is given by Child's law,

$$J_{SCLC} = \varepsilon\mu\frac{V^2}{L^3}. \tag{17}$$

Hence the range of bias in which $J \propto V^2$ is called the space charge limited current (SCLC) range [46].

There are many sources of shallow and deep traps in vacuum-evaporated small organic devices and spin-coated polymer devices. As the applied bias is increased, more currents are injected and fill the various trap-sites. The reduction in empty traps then causes a rapid increase in J with increasing V. The regime in which the current is limited by trap filling is called the trapped-charge limited (TCL) regime. At sufficiently high injection, the traps are filled and no longer limit carrier transport. This regime is called the trap-filled limit (TFL) regime. Thus the current in the TFL regime follows Child's law, i.e. $J \propto V^2$, because only shallow traps can release charges by thermal agitation.

One simple representation of the distribution of trap energies is the exponential distribution [45]

$$D_t(E) = D_{t0} e^{(E-E_{LUMO})/kT_t}, \tag{18}$$

where $D_t(E)$ is the concentration of traps per unit energy, D_{t0} is the trap concentration at the LUMO level, and $E_t = kT_t$ is a parameter characterizing the trap depth. For this distribution (Eq. (18)), the TCL current J_{TCL} is governed by a power law dependence on V; for unipolar electron transport [34]

$$J_{TCL} \approx q\mu_n N_{LUMO} \left(\frac{\varepsilon}{qD_{t0}E_t} \right)^l \frac{V^{l+1}}{L^{2l+1}}, \tag{19}$$

where $l = E_t / kT$, μ_n is the electron mobility, and N_{LUMO} is the density of states at the LUMO level. If $E_t << kT$, then the traps can be ignored ($l \approx 0$), and the current density J_{TCL} reduces to Ohmic behavior (Eq (14)). If $E_t \approx kT$, i.e. $l \approx 1$, the empty electron traps exist only at the top of the distribution (shallow traps), near the LUMO levels, and $J(V)$ follows Child's law

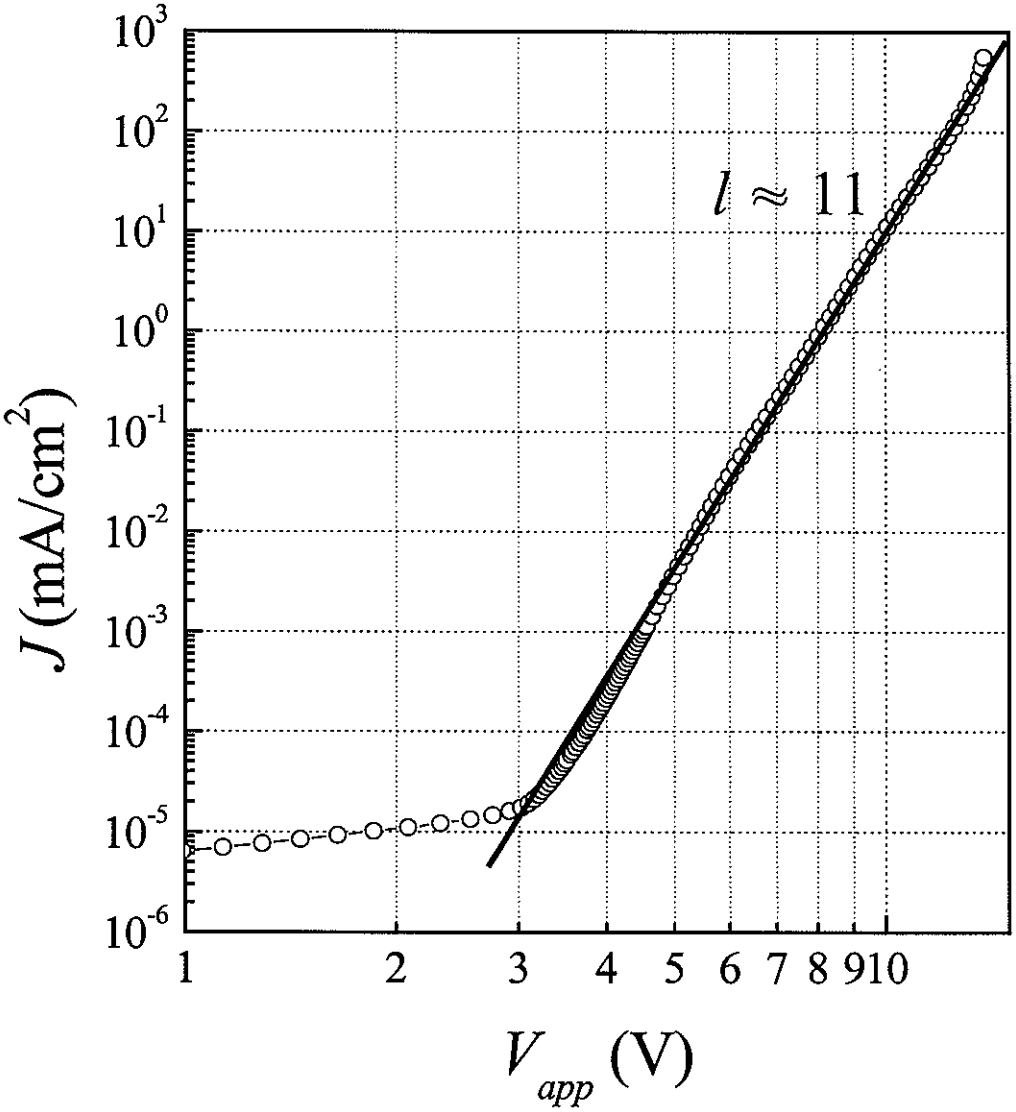

Figure 6. The *J-V* curve of an ITO/CuPc/α-NPD/DPVBi/Alq_3/CsF/Al OLED, a typical small molecular device. Note that the slope $l \approx 11$. At low voltage ($V_{app} < 3$ V), the actual current may be very different due to measurement system limitations. Note that the current density 10^{-5} mA/cm^2 corresponds to a total current of 0.17 nA.

($J \propto V^2$). The trap depth corresponding to $l \approx 1$ is still negligible because the charges trapped in these shallow traps are easily excited by thermal energy to generate free carriers.

Figure 6 shows a typical $J(V)$ curve of a small molecular OLED at room temperature on a log-log scale. As clearly seen, the slope is very steep ($l \approx 11$) at normal operating voltages. The estimated characteristic trap depth E_t under the assumption of an exponential trap distribution is ~ 0.28 eV. Up to at least 14 V, the behavior is trapped-charge limited (TCL). Hence, the traps are not fully filled by the injected carriers up to 14 V, as J_{TCL} varies by over 8 orders of magnitude, from ~ 10^{-5} mA/cm^2 (total current of 0.17 nA) at ~ 3 V and reaching up to ~ 10^3 mA/cm^2 (total current of 17 mA) at ~ 14 V.

Recombination and efficiency

When both electrons and holes are injected into luminescent organic materials, they can recombine to form various excited states such as singlet excitons, triplet excitons, and charge transfer excitons. In fluorescent devices, the emission is due to the radiative decay of singlet excitons (SEs), as radiative triplet exciton (TE) decay is forbidden.

Recombination

If the oppositely injected holes and electrons are statistically independent of each other and the recombination process is random, then it can be treated by the Langevin formalism [30,47]. To recombine, the separation $\lambda_{h\text{-}e}$ between the hole and the electron must be less than the Coulomb capture, or Onsager radius r_c (see Fig. 7). The definition of r_c is the distance where the Coulomb attractive energy and thermal dissociation energy are equal, i.e., [30]

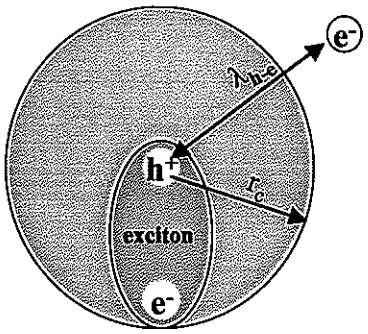

Figure 7. Mean separation $\lambda_{h\text{-}e}$ and Coulomb capture radius of a hole and electron pair. If $\lambda_{h-e} < r_c$, then the pair can form various excitons such as singlet, triplet, or charge transfer exciton.

$$r_c = \frac{q^2}{4\pi\varepsilon kT}. \tag{20}$$

Since $\varepsilon \sim 3\varepsilon_0$ for most organic materials, the typical capture radius is ~ 17 nm at room temperature. Hence, since efficient recombination requires $\lambda_{h\text{-}e} < r_c$, the charge carrier densities should be greater than 10^{17} cm^{-3}.

Electron-hole recombination is bimolecular. Hence its rate R is given by [30]

$$R = \gamma \cdot pn, \tag{21}$$

where p and n are the hole and electron densities, respectively, and $\gamma = e(\mu_h + \mu_e)/\varepsilon$ is the bimolecular recombination coefficient. For Alq_3, where the field-independent (or, equivalently, low field mobility) is $\mu_h+\mu_e \sim 10^{-7}$ cm^2/Vs and $\varepsilon \sim 3\varepsilon_0$, $\gamma \sim 10^{-13}$ cm^3/s. γ, of course, increases with increasing field [48].

Efficiency

If the recombination is Langevin type, and we assume that the probability of recombination of e^-–h^+ pairs in the singlet spin configuration to SEs is equal to the probability of recombination of pairs in the triplet spin configuration to TEs, then only a quarter of the pairs will recombine to the radiative SEs. Thus the internal EL efficiency or internal quantum efficiency (η_{EL}^{int}) will be limited to a maximum of 25 % when there is no quenching of SEs, and the hole-electron density is ideally balanced, i.e., $c_{h-e}=1$. However, typically, SEs are quenched by various processes such as charge transfer to another molecule, traps, and defects. Even if the material is excited by external photons, which generate only singlet excitons, the photoluminescence (PL) quantum yield η_{PL} of organic solids is typically less than 100 %. For example the yield of Alq_3 powder is ~ 32 % [34]. In electrical excitation, the internal EL quantum efficiency is written as

$$\eta_{EL}^{\text{int}} = c_{h-e}\eta_R\eta_{PL}, \tag{22}$$

where η_R is the fraction of recombination events that result in SEs; as noted above for random recombination $\eta_R = 25$ %.

Another very important device efficiency factor is the geometry of the device. Normally the organic layers are deposited on the ITO coated glass substrate. Hence, only the photons passing through the transparent substrate are collected by the detector. Due to the refractive index mismatch between the organic layers and ITO substrate, the rate and the direction of emission are strongly modified by optical interference effects [49]. These effects are quantified by the external coupling efficiency ξ, which depends on the direction of the dipole moment of the emitting molecules and the refractive index n of the emitting layer.

The coupling efficiency is estimated to be $\xi \approx 0.75/n^2$ for isotropic dipoles of the emitter, and $\xi \approx 1.2/n^2$ for in-plane dipoles [50]. Thus the external quantum efficiency η_{EL}^{ext} of the device is given by

$$\eta_{EL}^{ext} = \xi \eta_{EL}^{int}. \tag{23}$$

The typical value of n^2 is about 3 for the organic solids, so the maximum external quantum efficiency of Alq_3 devices is reduced to 2 – 3 %. Actual η_{EL}^{ext} of Alq_3 devices is typically ~ 1 % [2]. If η_{PL} of a given film is 100 %, the maximum possible η_{EL}^{ext} is limited 7 - 8 %, as long as the fraction of SEs is limited to 25 %.

Determination of η_{EL}^{ext} from brightness and current *vs.* applied voltage measurements

Direct measurement of η_{EL}^{ext} is very difficult and tricky. First, the light detector should be large enough to cover the whole hemisphere of the device emission. Second, the spectral response of the detector for different light intensity and colors must be known. Hence, instead of direct measurement, η_{EL}^{ext} is estimated indirectly from the brightness and emission spectrum. The brightness L of the device can be measured by a luminance meter and is typically expressed in Candela per unit area (Cd/m^2). At the same time the current density is measured at the given applied bias. Additionally, the emission spectrum $F(\lambda)$ is recorded for that bias. Using these data, η_{EL}^{ext} can be estimated based on the assumption that the spatial light distribution is Lambertian, i.e., cosine [51]

$$\eta_{EL}^{ext} = \frac{\pi e}{K_m hc} \frac{L}{J} \frac{\int F(\lambda) d\lambda}{\int \frac{F(\lambda) \cdot V(\lambda)}{\lambda} d\lambda}, \tag{24}$$

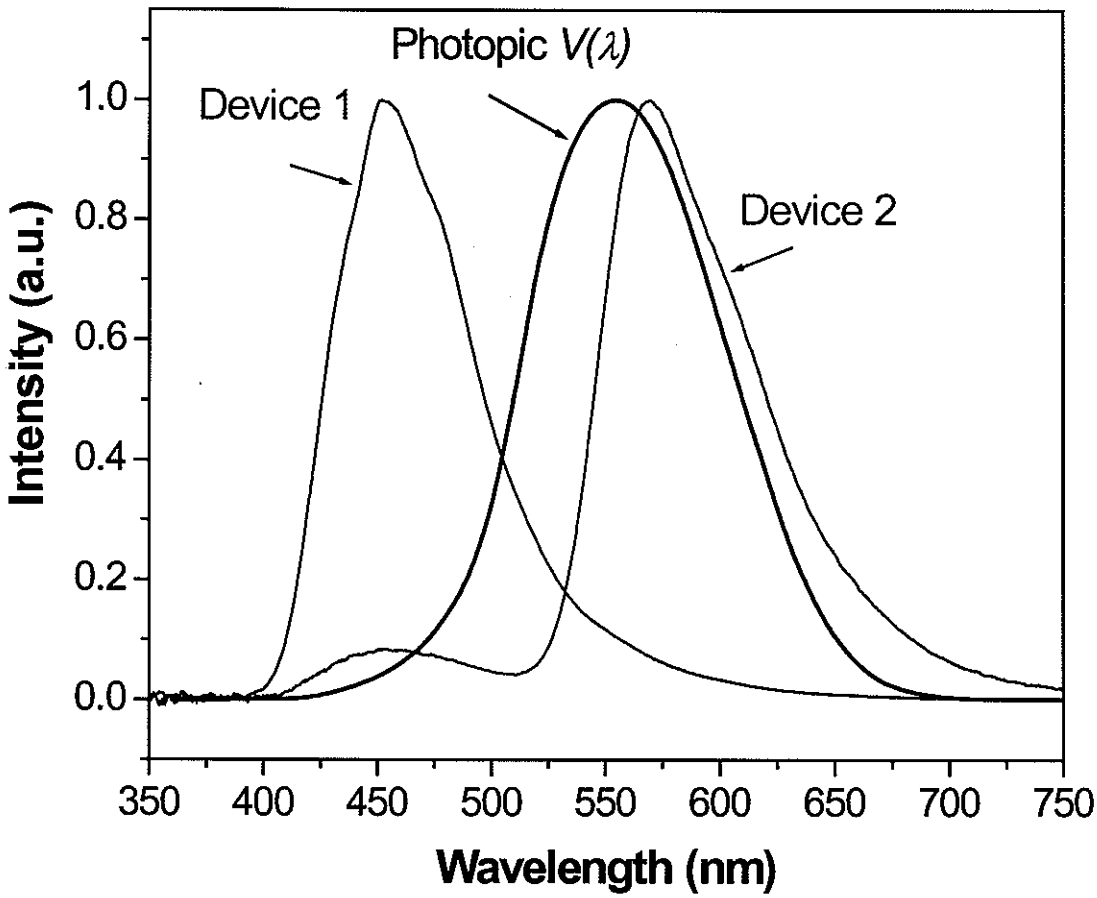

Figure 8. The photopic function $V(\lambda)$, which is the spectral response curve of the human eye, and is sensitive to yellowish-green (the peak is at 555 nm). The brightness L (in Cd/m^2) is determined from $V(\lambda)$; the luminance meter (Minolta model LS110) that was used in this work has a spectral response curve nearly identical to $V(\lambda)$. Even if the intensities of Device 1 and Device 2 are the same, the brightness can be very different due to $V(\lambda)$. In this figure Device 2 is brighter than Device 1 because the spectral overlap between Device 2 emission and $V(\lambda)$ is larger than that of Device 1.

where K_m =680 lm/W is the maximum luminous efficacy, and $V(\lambda)$ is the photopic spectral response of the human eye (see Fig. 8). The π in Eq. (24) is due to the Lambertian distribution.

Molecular doped guest-host system

To fabricate full color displays, red (R), green (G) and blue (B) pixels are needed, but it is difficult to fabricate red-emitting OLEDs with good charge conduction. Thus, all red-emitting devices incorporate luminescent dyes as dopant guest in host materials, and some devices also employ dopants for green and blue emission.

Molecular-doped guest-host (G-H) blends have been studied extensively to improve the efficiency [2,52] or to modify the emission color [53,54] of OLEDs. In general, the HOMO-LUMO energy gap of the guest molecule is smaller than that of the host, and at least one of the guest HOMO or LUMO levels is located inside the host HOMO-LUMO gap. Luminescent laser dye materials are often used as guests, e.g., the red-emitting 4-(dicyanomethylene)-2-methyl-6-(p-dimethyl aminostyryl)-4H-pyran (DCM1) and [2-methyl-6-[2-(2,3,6,7-tetrahydro-1H,5H-benzo[i,j]quinolizin-9-yl)ethenyl]-4H-pyran-4-ylidene]propane-dinitrile (DCM2). These guest materials are co-evaporated with the host, or the G-H blends are spin-coated when the host is a polymer.

There are three distinctive characteristics of guest dopants in OLEDs: First, the doped guest molecules act as strong charge trapping sites since at least one of the guest energy levels is located inside the HOMO-LUMO gap of the host. Second, they are very efficient fluorophores if doped at a low concentration. Third, it is very easy to modify the emission

colors of the OLEDs by controlling the doping parameters such as doping concentration and thickness of the G-H layer.

Extrinsic traps introduced by doping

If the HOMO or LUMO level of the doped molecules is inside the host energy gap, then the dopant generates extrinsic trap-sites. The current density will consequently be reduced by these traps at a given applied bias. With increasing trap density net mobile charge density decreases. In the example shown in Fig. 9(a), the hole traps [55] are generated by the 1-NaphDATA guest in the α-NPD host; the trap level was determined to be ~ 0.22 eV by thermally stimulated current (TSC) measurements. This value is in reasonable agreement with the energy difference between the guest and host HOMO which are 5.0 and 5.2 - 5.5 eV for 1-NaphDATA and α-NPD, respectively [55].

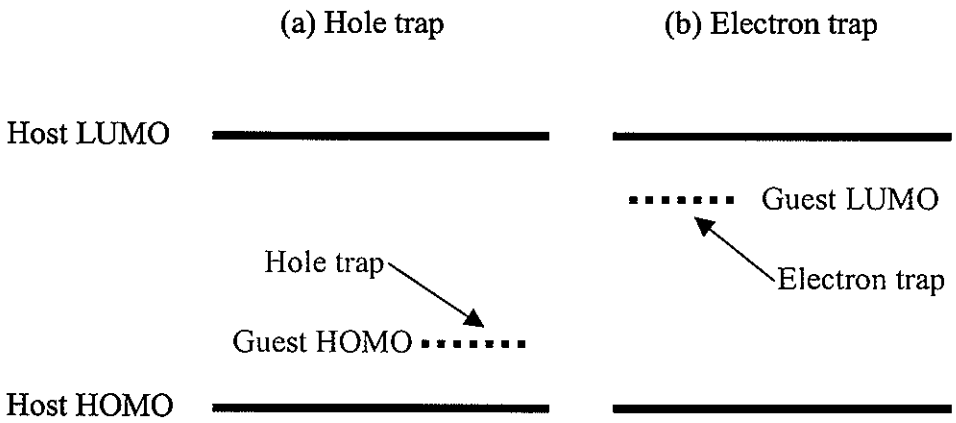

Figure 9. Schematic energy level diagram of a guest-host system with a hole and with an electron trap.

Energy transfer

In fluorescent G-H devices, the guest emission is usually due to Förster (or resonant) energy transfer from the donor host to the guest acceptor. A donor SE, or a host fluorophore, can transfer its energy to an acceptor (guest fluorophore) nonradiatively. The donor exciton induces an electric dipole on the acceptor molecule. The donor-acceptor dipole interaction (see Fig. 10) is proportional to R^{-6}, where R is the distance between the donor and acceptor molecules [30]. The energy transfer rate $K_{D\to A}$ [54] from the donor to the acceptor is given by

$$K_{D\to A} = \frac{1}{\tau_D}\left(\frac{R_0}{R}\right)^6, \tag{25}$$

where τ_D is the average donor exciton lifetime and R_0 is the energy transfer radius. R_0 is related to the overlap integral of the host donor emission $F_D(\omega)$ and guest acceptor absorption spectra $\sigma_A(\omega)$, and is given by

$$R_0 = \frac{3}{4\pi}\int \frac{c^4}{\omega^4 n^4} F_D(\omega)\sigma_A(\omega)d\omega, \tag{26}$$

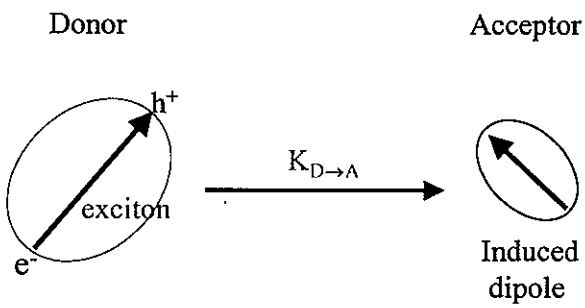

Figure 10. Förster (resonant) energy transfer mechanism from donor to acceptor fluorophore. The energy transfer rate is $K_{D\to A}$.

where n is the refractive index of the medium, and c is the speed of light in vacuum.

One of the popular G-H systems is DCM2-doped Alq_3, since the DCM2 guest is a strong emitter. Clearly, this emission depends on the doping concentration and doped-layer thickness. The calculated or measured energy transfer radii R_0 are 39 Å, 23 Å, and 32 Å for DCM2:Alq_3 [54], DCM2:α-NPD [56], and Alq_3:α-NPD system, respectively [56].

Besides Förster energy transfer, guest emission can also be generated by the recombination between an electron and a hole trapped on the guest. For example, DCM2 molecules are traps for both holes and electrons in Alq_3, α-NPD, and DPVBi hosts. Thus the guest molecule roles as a trap recombination center [2] to emit it's own color. If the trapped charge density is very high for both charges, then the recombination of trapped charges on guest molecules can generate efficient emission.

Device structures and materials

The chemical structures and full names of the materials used in this device are shown in Fig. 11. Figure 12(a) is a generic structure of a laser-dye-doped multilayer small molecular OLED that has fabricated and studied in this work. All organic materials and the cathode metal were evaporated by conventional thermal evaporation in a vacuum chamber ($<10^{-5}$ Torr) installed inside an Ar-filled glove box; the oxygen and water levels were normally below 1 ppm. The thickness of each layer was monitored by a Maxtek TM-100 thickness monitor. Typical deposition rates were 0.1 - 2 Å/sec for the organic materials, and 2 – 3 Å/sec for the Al cathode.

To fabricate the devices, 2"×2" ITO substrates were aquaregia-treated to improve hole injection. On the treated ITO, a ~ 5 nm thick layer of the blue pigment copper

(a)

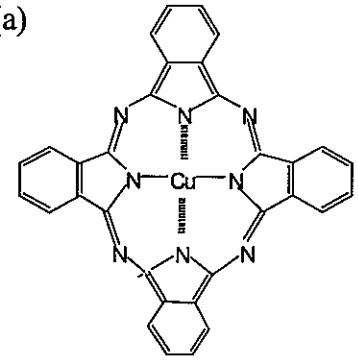

Copper phthalocyanine (CuPc)

(c)

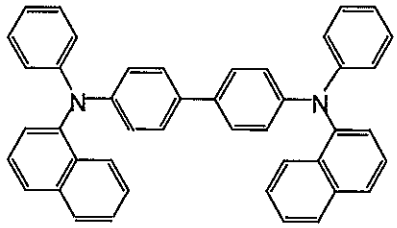

N,N'-diphenyl-N,N'-bis(1-naphthylphenyl)-1,1'-biphenyl-4,4'-diamine (α-NPD)

(d)

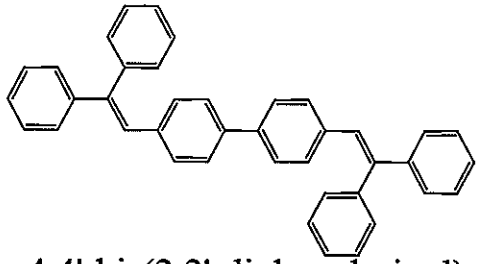

4,4'-bis(2,2'-diphenyl-vinyl) -1,1'-biphenyl (DPVBi)

(b)

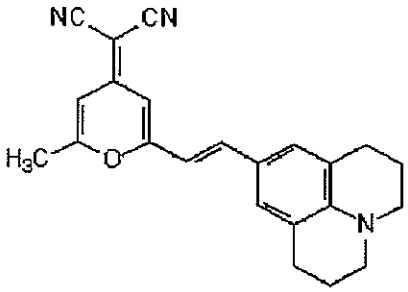

2-methyl-6-[2-(2,3,6,7-tetrahydro-1H,5H-benzo[i,j]quinolizin-9-yl) ethenyl]-4H-pyran-4-ylidene]propane-dinitrile (DCM2)

(e)

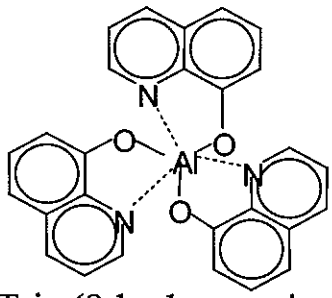

Tris-(8-hydroxyquinoline) aluminum (Alq_3)

Figure 11. Molecule structures and full names of the materials used in this work.

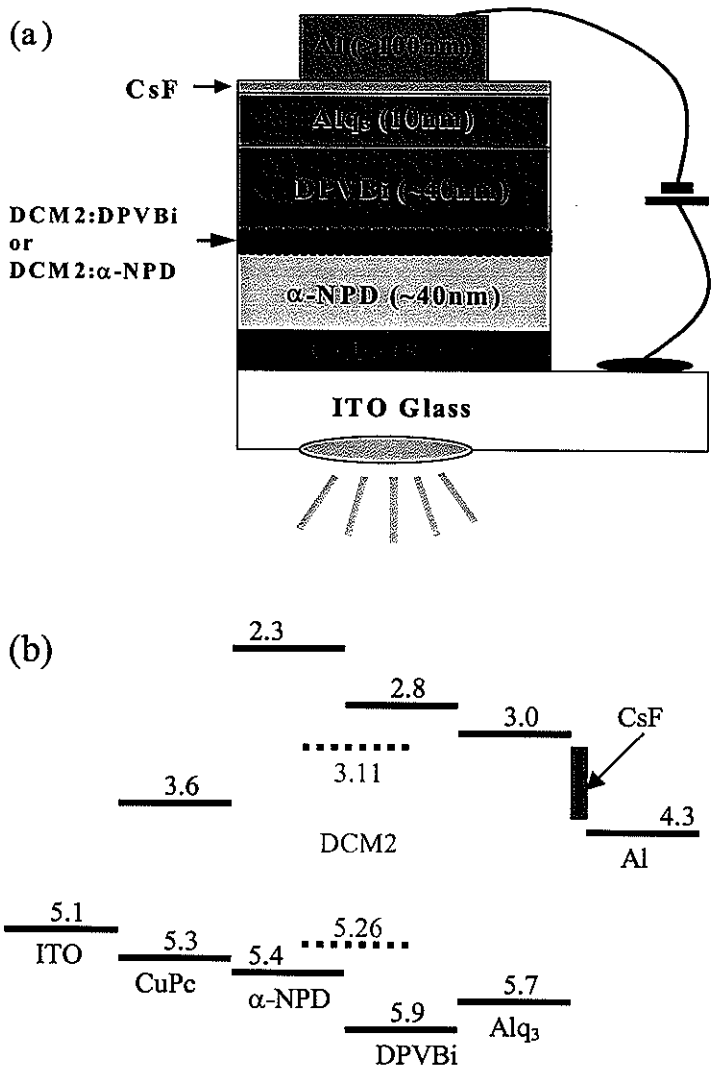

Figure 12. (a) Typical multilayer device structure studied in this study. DCM2 is doped at various doping concentrations and thicknesses in either the α-NPD HTL or the DPVBi emitting layer. (b) Energy level diagram of the structure. CsF lowers the electron injection barrier, but the degree of lowering is unknown.

phthalocyanine (CuPc) was deposited. The ~ 5.3 eV HOMO level of CuPc is close to the ~ 5.1 eV Fermi level of ITO (see the energy diagram in Fig. 12(b)), so efficient hole carrier injection from ITO in CuPc is expected. In addition, CuPc is known to be a good hole conductor, with hole mobility 0.02 – 0.04 cm^2/Vs at room temperature [57].

Following the deposition of CuPc, 40 nm thick hole transport layer (HTL) of N,N'-diphenyl-N,N'-bis(1-naphthylphenyl)-1,1'-biphenyl-4,4'-diamine (α-NPD) was deposited. The thermal stability of α-NPD is greater than that of the traditional N,N'-Bis-(3-Methylphenyl)-N,N'-bis-phenyl (TPD), since the glass transition temperature T_g of α-NPD is $95^{\circ}C$, whereas TPD is $65^{\circ}C$ [58]. The hole mobility of α-NPD is ~ $3\times10^{-4}\,cm^2/Vs$ at typical operating voltages [59].

For emission, a layer of highly efficient blue fluorescent 4,4'-bis(2,2'-diphenyl-vinyl)-1,1'-biphenyl (DPVBi) [60] was evaporated on the α-NPD. DPVBi is a distyrylarylene derivative; its emission peaks at 460 nm, and it forms smooth and flat thin films free of pinholes [61]. It is a relatively well planarized molecule, so the intermolecular distance of 4 –5 Å [61] is quite small compared to the intermolecular distance of 8 Å between Alq_3 molecules [61]. In the trap-limited regime, the estimated electron mobility in DPVBi is ~ 3 times less than in Alq_3 [62]. As shown in Fig. 12(b), there are very large energy level offsets between α-NPD and DPVBi for electrons and holes; due to these large offsets charge accumulation builds up around α-NPD/DPVBi interface, and the recombination zone is consequently located there. In this work, DCM2 was usually co-evaporated with α-NPD or DPVBi. The doping parameters depended on the goals of the study, which are described in detail in each chapter.

To protect the DPVBi layer from the relatively high temperature during the subsequent evaporation Al, a 10 nm thick electron transport Alq_3 layer was evaporated between the DPVBi and Al layer, since, Alq_3 has a very high $T_g > 170°C$ [63], in contrast to the $T_g = 64°C$ of DPVBi [64]. The thickness of the Alq_3 layer was limited to 10 nm to avoid emission from Alq_3.

On the top of the Alq_3 layer, a very thin 1 nm-thick CsF layer was deposited to improve electron injection from the ~ 150 nm thick Al cathode. The Al was deposited for external contact through a 2"×2" mask containing 21×21 hole pixels; the holes were ~ 1.5 mm in diameter.

Dissertation organization

This dissertation consists mainly of papers published, submitted, or prepared for submission to forefront international journals.

Chapter 1 provided a general introduction and described the basic properties of OLEDs. It included carrier transport, recombination mechanisms, and a brief description of molecular doped guest-host systems. Chapter 2 is an article published in Applied Physics Letters. Very bright white OLEDs (WOLEDs) are described in this paper. The maximum brightness exceeded 50,000 Cd/m^2, with a very high quantum efficiency. Chapter 3 is a manuscript submitted to Applied Physics Letters. The chapter describes a novel method to modify the emission colors of OLEDs. It shown that not only the doping concentration, but also the doping thickness, is very important in determining the emission color of doped guest-host devices. Chapter 4 is a manuscript that will be submitted to Applied Physics Letters, in which the energy transfer mechanism from host to guest is described. The energy transfer

radius in selective guest-host systems is determined from systematic measurements and well-established models. Chapter 5 describes the turn-off dynamics of devices, using a new recombination model. This chapter will be submitted for publication in Physical Review Letters. The study shows that the turn-off dynamics are strongly affected by charge traps in the recombination zone. Finally, Chapter 6 presents the general conclusions and a summary of this work.

References

[1] C. W. Tang and S. A. VanSlyke, Appl. Phys. Lett. **51**, 913 (1987).

[2] C. W. Tang, S. A. VanSlyke, and C. H. Chen, J. Appl. Phys. **65**, 3610 (1989).

[3] L. Zou, V. Savvate'ev, J. Booher, C.-H. Kim, and J. Shinar, Appl. Phys. Lett. **79**, 2282 (2001); Alex K-Y. Jen, Yunqi Liu, Qiao-Sheng Hu, and Lin Pu, Appl. Phys. Lett. **75**, 3745 (1999).

[4] H. Suzuki, Appl. Phys. Lett. **80**, 3256 (2002).

[5] M. Pope, H. P. Kallmann, and P. Magnante, J. Chem. Phys. **38**, 2042 (1963); M. Sano, M. Pope, and H. Kallmann, J. Chem. Phys. **43**, 2920 (1965).

[6] W. Helfrich and W. G. Schneider, Phys. Rev. Lett. **14**, 229 (1965); W. Helfrich and W. G. Schneider, J. Chem. Phys. **44**, 2902 (1965).

[7] P. S. Vincett, W. A. Barlow, R. A. Hann, and G. G. Roberts, Thin Solid Films **94**, 171 (1982).

[8] C. Adachi, S. Tokito, T. Tsutsui, and S. Saito, Jap. J. Appl. Phys. **27**, L269 (1988); C. Adachi, S. Tokito, T. Tsutsui, and S. Saito, Jap. J. Appl. Phys. **27**, L713 (1988).

[9] J. H. Burroughes, D. D. C. Bradley, A. R. Brown, R. N. Marks, K. Mackay, R. H. Friend, P. L. Burns, and A. B. Holmes, Nature **347**, 539 (1990).

[10] S. Hotta and K. Waragai, Adv. Mater. **5**, 896 (1993).

[11] F. Garnier, R. Hajlaoui, A. Yassar, and P. Srivastava, Science **265**, 1684 (1994); T. R. Hebner, C. C. Wu, D. Marcy, M. H. Lu, and J. C. Sturm, Appl. Phys. Lett. **72**, 519 (1998); J. Bharathan and Y. Yang, Appl. Phys. Lett. **72**, 2660 (1998).

[12] M. A. Baldo, D. F. O'Brien, Y. You, A. Shoustikov, S. Sibley, M. E. Thompson, and S. R. Forrest, Nature **395**, 151 (1998); C. Adachi, M. A. Baldo, M. E. Thompson, and S. R. Forrest, J. App. Phys. **90**, 5048 (2001).

[13] P. W. Wang, Y. J. Lui, C. Devadoss, P. Bharathi, and J. S. Moore, Adv. Mater. **8**, 237 (1996).

[14] J. N. G. Pillow, M. Halim, J. M. Lupton, P. L. Burn, and I. D. W. Samuel, Macromolecules **32**, 5985 (1999).

[15] J. M. Lupton, I. D. W. Samuel, R. Beavington, M. J. Frampton, P. L. Burn, and H. Bässler, Phys. Rev. B **63**, 155206 (2001)

[16] J. Shi and C. W. Tang, Appl. Phys. Lett. **70**, 1665 (1997); V.-E. Choong, S. Shi, J. Curless, C.-L. Shieh, H.-C. Lee, F. So, J. Shen, and J. Yang, Appl. Phys. Lett. **75**, 172 (1999).

[17] H. Kim, C. M. Gilmore, A. Piqué, J. S. Horwitz, H. Mattoussi, H. Murata, Z. H. Kafafi and D. B. Chrisey, J. Appl. Phys. **86**, 6451 (1999).

[18] F. Li, H. Tang, J. Shinar, O. Resto, and S. Z. Weisz, Appl. Phys. Lett. **70**, 2741 (1997).

[19] D. J. Milliron, I. G. Hill, C. Shen, A. Kahn, and J. Schwartz, J. Appl. Phys. **87**, 572 (2000).

[20] F. Nüesch, E.W. Forsythe, Q. T. Le, Y. Gao, and L. J. Rothberg, J. Appl. Phys. **87**, 7973 (2000); C. Hosokawa, H. Higashi, H. Nakamura, and T. Kusumoto Appl. Phys. Lett. **67**, 3853 (1997).

[21] H. Ishii, K. Sugiyama, E. Ito, and K. Seki, Adv. Mater. **11**, 605 (1999).

[22] K. Sugiyama, H. Ishii, Y. Ouchi, and K. Seki, J. Appl. Phys. **87**, 297 (2000).

[23] P. He, S. D. Wang, W. K. Wong, C. S. Lee, and S. T. Lee, Appl. Phys. Lett. **79**, 1561 (2001).

[24] S. M. Sze, *Physics of Semiconductor Devices*, John Wiley & Sons.

[25] H.Suzuki, Appl. Phys. Lett. **69**, 1611 (1996). F. Li, H. Tang, J. Anderegg, and J. Shinar, Appl. Phys. Lett. **70**, 1233 (1997). H. Aziz, Z. Popovic, C. P. Tripp, N. Hu, A. Hor, and G. Xu, Appl. Phys. Lett. **72**, 2642 (1998). G. E. Jabbour, B. Kippelen, N. R. Armstrong, and N. Peyghambarian, Appl. Phys. Lett. **73**, 1185 (1998). T. M. Brown, J. S. Kim, R. H. Friend, F. Cacialli, R. Daik, and W. J. Feast, Appl. Phys. Lett. **75**, 1679 (1999). P. E. Burrows, G. Gu, S. R. Forrest, E. P. Vicenzi, T. X. Zhou, J. Appl. Phys. **87**, 3080 (2000). P. Piromreun, H. Oh, Y. Shen, G. G. Malliaras, J. C. Scott, and P. J. Brock, Appl. Phys. Lett. **77**, 2403 (2000). W. Brütting, H. Riel, T. Beierlein, and W. Riess, J. Appl. Phys. **89**, 1704 (2001). T. M. Brown, R. H. Friend, I. S. Millard, D. J. Lacey, J. H. Burroughes, and Cacialli, Appl. Phys. Lett. **79**, 174 (2001). A. Turak, D. Grozea, X. D. Feng, Z. H. Lu, H. Aziz, and A. M. Hor, Appl. Phys. Lett. **81**, 766 (2002).

[26] G. Greczynski, M. Fahlman, and W. R. Salaneck, J. Chem. Phys. **114**, 8628 (2001)

[27] V.-E. Choong, Y. Park, Y. Gao, T. Wehrmeister, K. Müllen, B. R. Hsieh, and C. W. Tang, J. Vac. Sci. Technol. A **15**, 1745 (1997).

[28] A. Sussman, J. Appl. Phys. **38**, 2738 (1967); A. J. Campbell, D. D. C. Bradley, and D. G. Lidzey, J. Appl. Phys. **82**, 6326 (1997); J. Shen and J. Yang, J. Appl. Phys. **83**, 7706 (1998).

[29] C. Kittel, Introduction to Solid State Physics, 6th ed., John Willey & Sons. (1986).

[30] M. Pope and C. E. Swenberg, *Electronic Processes in Organic Crystals* (Oxford

University Press, Oxford, 1982).

[31] S. A. Elnahwy, M. El Hamamsy, and A. C. Damask, Phys. Rev. B **19** 1108 (1979); K. Hummer, P. Puschnig, and C. Ambrosch-Draxl, Phys. Rev. B **67**, 184105 (2003).

[32] J. H. Schön, Ch. Kloc, and B. Batlogg, Phys. Rev. B **63**, 245201 (2001).

[33] E. M. Conwell, Phys. Rev. B **22**, 1761 (1980); N. Ueno, K. Sugita, and T. Shinmura, Phys. Rev. B **44**, 6472 (1991).

[34] P. E. Burrows, Z. Shen, V. Bulovic, D. M. McCarty, S. R. Forrest, J. A. Cronin, and M. E. Thompson, J. Appl. Phys. **79**, 7991 (1996).

[35] A. V. Vannikov, A. D. Grishina, and S. V. Novikov, Russian Chemical Reviews **63**, 103 (1994).

[36] H. Bässler, Phys. Stat. Sol. (b) **175**, 15 (1993).

[37] K. Waragai, H. Akimichi, S. Hotta, H. Kano, and H. Sakaki, Phys. Rev. B **52**, 1786 (1995).

[38] M. Stolka, J. F. Yanus, and D. M. Pai, J. Phys. Chem. **88**, 4707 (1984); J. Kalinowski, J. Phys. D: Appl. Phys. **32**, R179 (1999); E. W. Forsythe, M. A. Abkowitz, Y. Gao, and C. W. Tang, J. Vac. Sci. Technol. A **18**, 1869 (2000).

[39] B. J. Chen, W. Y. Lai, Z. Q. Gao, C. S. Lee, S. T. Lee, and W. A. Gambling, Appl. Phys. Lett. **75**, 4010 (1999); R. G. Kepler, P. M. Beeson, S. J. Jacobs, R. A. Anderson, M. B. Sinclair, V. S. Valencia, and P. A. Cahill, Appl. Phys. Lett. **66**, 3618 (1995).

[40] I. H. Campbell and D. L. Smith, Appl. Phys. Lett. **74**, 561 (1999).

[41] E. Tutis, M.-N. Bussac, and L. Zuppiroli, Appl. Phys. Lett. **75**, 3880 (1999).

[42] P. S. Davids, I. H. Campbell, and D. L. Smith, J. Appl. Phys. **82**, 6319 (1997).

[43] A. J. Campbell, D. D. C. Bradley, J. Laubender, and M. Sokolowski, J. Appl. Phys. **86**, 5004 (1999).

[44] M. A. Baldo and S. R. Forrest, Phys. Rev. **B 64**, 85201 (2001).

[45] M. A. Lampert and P. Mark, *Current Injection in Solids*, Academic Press (1970).

[46] D. J. Pinner, R. H. Friend, and N. Tessler, J. Appl. Phys. **86**, 5116 (1999).

[47] U. Albrecht and H. Bässler, Phys. Stat. Sol. (b) **191**, 455 (1995).

[48] I. Sokolik, R. Priestley, A. D. Walser, R. Dorsinville, and C. W. Tang, Appl. Phys. Lett. **69**, 4168 (1996).

[49] M.-H. Lu and J. C. Sturm, J. Appl. Phys. **91**, 595 (2002).

[50] J. S. Kim, P. K. H. Ho, N. C. Greenham, and R. H. Friend, J. Appl. Phys. **88**, 1073 (2000).

[51] D. O'Brien, A. Bleyer, D. G. Lidzey, and D. D. C. Bradley, T. Tsutsui, J. Appl. Phys. **82**, 2662 (1997).

[52] B. W. D'Andrade, M. A. Baldo, C. Adachi, J. Brooks, M. E. Thompson, and S. R. Forrest, Appl. Phys. Lett. **79**, 1045 (2001).

[53] Y. Hamada, H. Kanno, T. Tsujioka, H. Takahashi, and T. Usuki, Appl. Phys. Lett. **75**, 1682 (1999).

[54] V. Bulović, A. Shoustikov, M. A. Baldo, E. Bose, V.G. Kozlov, M. E. Thompson, and S. R. Forrest, Chem. Phys. Lett. **287**, 455 (1998).

[55] N. von Malm, J. Steiger, R. Schmechel, and H. von Seggem, J. Appl. Phys. **89**, 5559 (2001).

[56] R. S. Deshpande, V. Bulović, and S. R. Forrest, Appl. Phys. Lett., **75**, 888 (1999).

[57] A. Sussman, J. Appl. Phys. **38**, 2738 (1967).

[58] J. Shinar and V. Savvateev, in *Organic Light Emitting Devices*, edited by J. Shinar, Chapter 1, Springer Verlag, NY (2003).

[59] E. W. Forsythe, M. A. Abkowitz, Y. Gao, and C. W. Tang, J. Vac. Sci. Tech. A **18**, 1869 (2000).

[60] C. Hosokawa, H. Higashi, H. Nakamura, and T. Kusumoto, Appl. Phys.Lett. **67**, 3853 (1995); C. Hosokawa, M. Eida, M. Matsuura, K. Fukuoka, and H. Nakamura, T. Kusumoto, Synth. Met., **91** (1997); S. E. Shaheen, G. E. Jabbour, M. M. Morrell, Y. Kawabe, B. Kippelen, N. Peyghambarian, M.-F. Nabor, R. Schlaf, E. A. Mash, and N. R. Armstrong, J. Appl. Phys. **84**, 2324 (1998); H. Spreitzer, H. Schenk, J. Salbeck, F. Weissoertel, H. Riel, and W. Riess, Proc. SPIE Vol. **3797**, 316 (1999).

[61] H. S. Karlsson, K. Read, R. Haight, J. Vac. Sci. Technol. A **20**, 762 (2002).

[62] E. I. Haskal, Synth. Met. **91**, 187 (1997).

[63] D. F. O'Brien, P. E. Burrows, S. R. Forrest, B. E. Koene, D. E. Loy, and M. E. Thompson, Adv. Mat. **10**, 1108 (1998).

[64] H. Spreitzer, H. Schenk, J. Salbeck, F. Weissoertel, H. Riel, and W. Reiss, in *Organic Light Emitting Materials and Devices III,* edited by Z. H. Kafafi, Proc. SPIE **3797**, 316 (SPIE, Bellingham, WA, 1999).

2. BRIGHT WHITE SMALL MOLECULAR ORGANIC LIGHT-EMITTING DEVICES BASED ON RED-EMITTING GUEST-HOST LAYER AND BLUE-EMITTING 4,4'-BIS(2,2'-DIPHENYLVINYL)-1,1'-BIPHENYL

A paper published in Applied Physics Letters **81**, 1783 (2002)

K. O. Cheon and J. Shinar

Abstract

Bright multilayer white organic light-emitting devices (OLEDs) based on red-emitting [2-methyl-6-[2-(2,3,6,7-tetrahydro-1H,5H-benzo[i,j]quinolizin-9-yl)ethenyl]-4H-pyran-4-ylidene]propane-dinitrile (DCM2)-doped N,N'-diphenyl-N,N'-bis(1-naphthylphenyl)-1,1'-biphenyl-4,4'-diamine (α-NPD) and blue-emitting 4,4'-bis(2,2'-diphenylvinyl)-1,1'-biphenyl (DPVBi) are described. The blue emission increased relative to the red emission band with increasing bias, but the color coordinates of the total emission were well within the white region at $V > 10$ V. The most lightly doped device, which contained a 5 nm thick layer of 0.5 wt. % of the dye dopant, exhibited the highest power efficiency, 4.1 lm/W, external quantum efficiency of 3.0 %, and white brightness $L_{max} > 50{,}000$ Cd/m^2 (at 1,100 mA/cm^2).

Introduction

Multicolor organic light emitting devices (OLEDs) have undergone dramatic improvements in efficiency and brightness [1,2,3,4,5] following the demonstration of color tuning or the organic devices using luminescent dyes as dopants [1]. White OLEDs

(WOLEDs) have attracted particular attention not only as a light source for liquid-crystal displays [6] but also as candidates for next generation lighting; the maximal brightness of WOLEDs reported to date is 25,000 Cd/m^2 [7]. While this brightness is impressive, the efficiency of these WOLEDs is lower than that of single-emitting-layer devices.

Many of the WOLEDs described to date were modified from the [N,N'-diphenyl-N,N'-bis(1-naphthylphenyl)-1,1'-biphenyl-4,4'-diamine (α-NPD)]/[tris(8-hydroxy quinoline) Al (Alq_3)] structure [2]. Red, green, and blue emission bands are generally needed to generate white emission. However, it is difficult to fabricate red-emitting layers with good charge conduction. Hence red-emitting dye-doped layers have become attractive for this purpose. Both red-emitting 4-(dicyano-methylene)-2-methyl-6-(p-dimethyl aminostyryl)-4H-pyran (DCM1)- or {[2-methyl-6-[2-(2,3,6,7-tetrahydro-1H, 5H-benzo [ij] quinolizin-9-yl)-ethenyl)-4H-pyran-4-ylidene] propane-dinitrile} (DCM2)-doped α-NPD hole transporting layers or Alq_3 electron transport layers have been reported [1,2,7]. The emission spectra of the DCM2-doped devices redshift with increasing concentration n_{DCM2} in an organic solid, due to the solid state solvation effect (SSSE) [2].

In general, the emission spectra of the organic materials are very broad compared to inorganic LEDs. These broad spectra may yield white emission based on only two bands such as blue and orange. Then the number of emitting layers is reduced accordingly from three to two.

An efficient guest–host system is usually fabricated using highly radiative guest molecules with highest occupied molecular orbital (HOMO) and lowest unoccupied molecular orbital (LUMO) levels inside the HOMO–LUMO gap of the host, e.g. DCM2: α-NPD and DCM2:Alq_3 . Most of the guest emission is then due to Förster energy transfer of

the singlet exciton energy from the host to the guest. In addition to this energy transfer, interlayer Förster energy transfer is also possible [2], if the emission energy of the adjacent layer overlaps the guest absorption band. To generate white emission, the interlayer energy transfer is controlled by inserting an extra blocking layer [2,8]. This blocking layer is necessary for color tailoring, but it may imbalance the electron and hole injection rates, or the current may decrease at that bias. These effects will reduce the device performance parameters, e.g., lower the power efficiency or increase the operating voltage.

Device structures and Experiments

This study describes the properties of OLEDs in which the blue-emitting layer of highly luminescent 4,4'-bis(2,2'-diphenylvinyl)-1,1'-biphenyl (DPVBi) [3,9-11], was deposited directly above the DCM2-doped- α-NPD orange- to red-emitting layer. These devices, with no blocking layer between the two emitters, exhibited power efficiencies η_{power} reaching 4.1 lm/W, external quantum efficiencies η_{ext} reaching 3.0% at 1,000 Cd/m^2, and maximal brightness that exceeded 50,000 Cd/m^2. Their fabrication procedure was similar to that of OLEDs described elsewhere [12,13]. All the depositions were performed by conventional thermal evaporation in a vacuum chamber (< 10^{-5} Torr) installed inside a glove box with less than 1 ppm of water and oxygen. The deposition rates of the layers were 1–3 Å/s. A 5 nm thick copper phthalocyanine layer was deposited directly above the indium tin oxide anode to improve hole injection, followed by a 35 or 40 nm thick α-NPD hole transport layer. For red or orange emission, a 0, 5, or 10 nm-thick layer of DCM2-doped α-NPD was deposited on the neat α-NPD layer by coevaporation of the two source materials; the proper ratio of the

evaporation rates of the DCM2 and α-NPD was assumed to result in 0.5, 1, 2, and 5 wt% DCM2: α-NPD (see Table I). To generate blue emission, a 40 nm thick DPVBi was deposited on the DCM2: α-NPD layer, followed by a 10 nm thick Alq_3 electron transporting layer. The Alq_3 layer was followed by a ~ 1 nm thick CsF buffer layer to improve the electron injection from the 150 nm thick Al cathode layer. In order to minimize the role of uncontrolled deposition parameters which vary from batch to batch, Devices 1 to 3 were fabricated at the same time using a sliding shutter technique [14]. Devices 4 to 6 were similarly fabricated at the same time. The active sample area of each OLED pixel was 1.8 mm^2. The brightness was determined using a Minolta LS110 luminance meter and/or a Hamamatsu 3456 photomultiplier tube (PMT), while the photoluminescence (PL) and electroluminescence (EL) spectra were obtained using an Ocean Optics CHEM2000 integrated spectrometer.

Experimental results and discussions

Figure 1 shows typical emission spectra of the devices; the arrows indicate the peak emission wavelengths of the PL of pure α-NPD, DPVBi, and solid DCM2. The PL spectrum of Device 3 (open squares) peaks at 445 nm, due to α-NPD, but also includes a weaker peak at 570 nm, due to DCM2. All of the other devices exhibited a similar PL spectrum, but, as expected, the 570 nm band increased and redshifted with increasing DCM2 concentration. However, in all of the devices, the blue EL band is redshifted to 460 nm from the 445 nm PL band of Device 3, indicating that it is due to emission from the DPVBi layer.

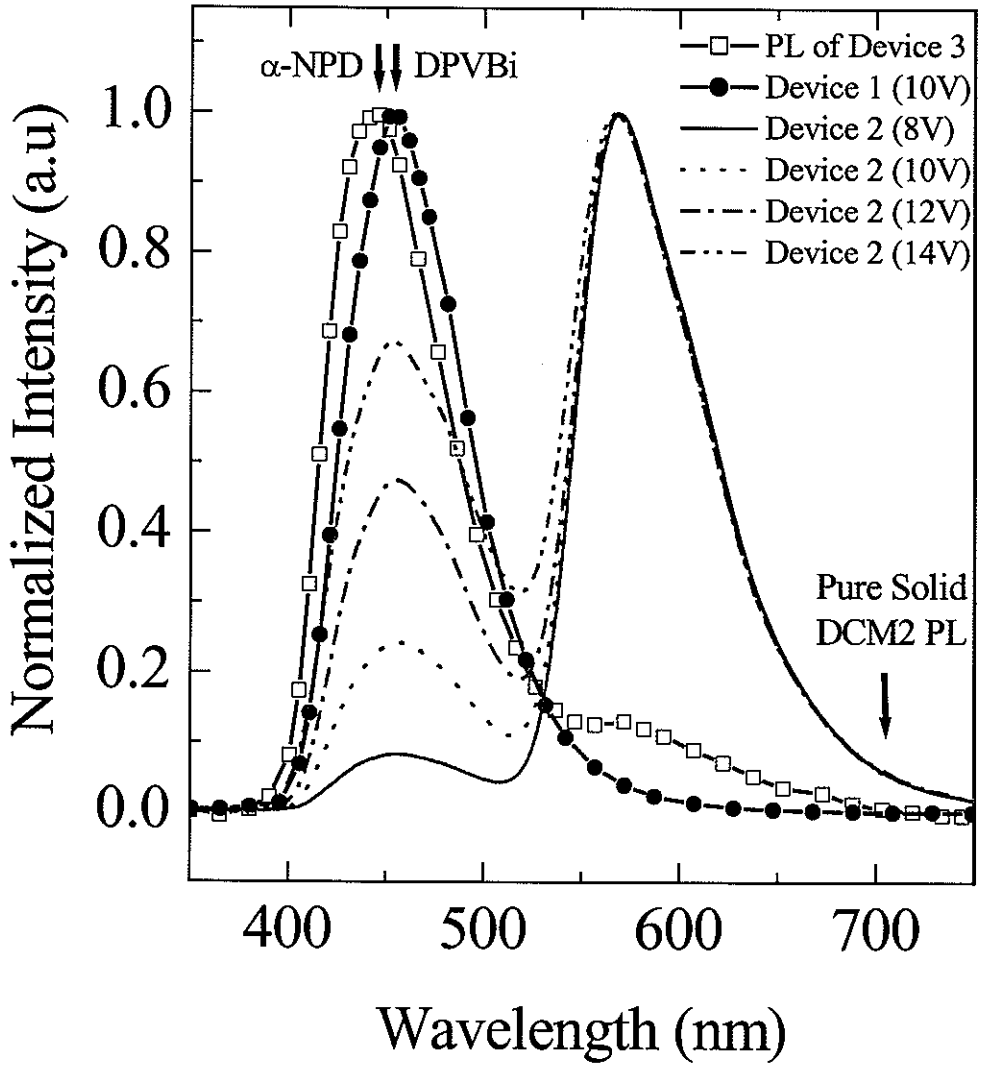

Figure 1. Normalized PL spectrum of Device 4 (open squares), EL spectrum of Device 1 at 10V (open circles), and the EL spectra of Device 2 biased at 8, 10, 12, and 14 V (solid and dashed lines).

The lines in Fig. 1 show the EL spectra of Device 2 at different bias voltages V. The observed increase of the DPVBi emission band with increasing V emission is very strong and typical of multicolor emission devices with no blocking layer to control the energy transfer.

The 570 nm DCM2 emission band redshifted with increasing dye concentration in α-NPD. As mentioned above, this is due to the SSSE.[2] Indeed, while the PL of pure solid DCM2 peaks at 705 nm, the EL of 0.5 wt.% DCM2: α-NPD peaks at 570 nm, i.e., at a photon energy which is 0.4 eV higher. In Device 6, with 5 wt.% DCM2: α-NPD, the DCM2 emission peaked at 632 nm.

TABLE I. DCM2 doping level (in wt. %) and thickness t of the DCM2:α-NPD layer, and the current density J,[a] power efficiency η_{power},[a] external quantum efficiency η_{ext} (%), CIE coordinates[b] at V = 12 V, and maximum brightness L_{max} of the OLEDs.

	Device 1	Device 2	Device 3	Device 4	Device 5	Device 6
Doping level	0	0.5	0.5	1	2	5
t	0	5	10	10	10	10
J (mA/cm^2)[a]	31	13	15	20	45	272
η_{power} (lm/W)[a]	1.0	2.4	2.0	1.5	0.6	0.08
η_{ext} (%)[a]	3.5	3.0	2.6	2.1	1.1	0.3
Color coordinates[b]	(0.15, 0.15)	(0.40, 0.37)	(0.42, 0.38)	(0.44, 0.38)	(0.54, 0.40)	(0.58, 0.37)
L_{max} (Cd/m^2)	21,000	54,000	30,000	20,000	11,000	2,300

[a]At 1000 Cd/m^2.
[b]At a bias 12 V.

Figure 2 shows the color coordinates of all of the devices at $V \geq 5$ V. As in Device 2, the coordinates of all of the OLEDs blue shifted with increasing V; even the undoped Device 1 exhibited a slight color variation with V which saturated at color coordinates (0.15, 0.15).

At very low voltage, all of the devices exhibited the DCM2 emission only. The paths shown in Fig. 2 start from different CIE coordinates due to the SSSE. With increasing voltage, all doped samples evolved toward the white (0.33, 0.33) coordinates. Device 2, with a thin 5 nm thick 0.5 wt.% DCM2: α-NPD, exhibited the "whitest" CIE coordinate, (0.36, 0.35), at 11 V.

Figure 3 shows the current density J of the devices versus the average applied electric-field $F = V/t_{tot}$, where t_{tot} is the total thickness of the organic layers; the built-in potential is ignored. At fixed F, J generally decreases with increasing DCM2 concentration. At $F = 1.2$ MV/cm, the current density of Device 6 is only 25% of the neat Device 1. It is known that α-NPD is a trap-free hole transport material [15,16]; hence, the DCM2 traps holes at its HOMO level ($E_{HOMO} = 5.26$ eV) [17] which is higher than that of α-NPD ($E_{HOMO} = 5.5$ eV) [18]. These traps clearly reduce the hole mobility in that layer, reducing J at a given F.

The brightness L of the samples is shown in the inset Fig. 3. The maximum values L_{max} were 21,000, 54,000, 30,000, 20,000, 11,000, and 2,300 Cd/m^2 for Devices 1–6, respectively (see Table I). Devices 2 and 3, with 0.5 wt.% DCM2: α-NPD, were brighter than the neat Device 1 over the entire operating range of F, while Devices 4–6, with higher n_{DCM2}, were less bright.

Figures 4(a) and 4(b) show the power efficiency η_{power} (in lumens/W) and external quantum efficiency η_{ext}, respectively. Device 2 exhibited the highest η_{power} of 4.1 lm/W at

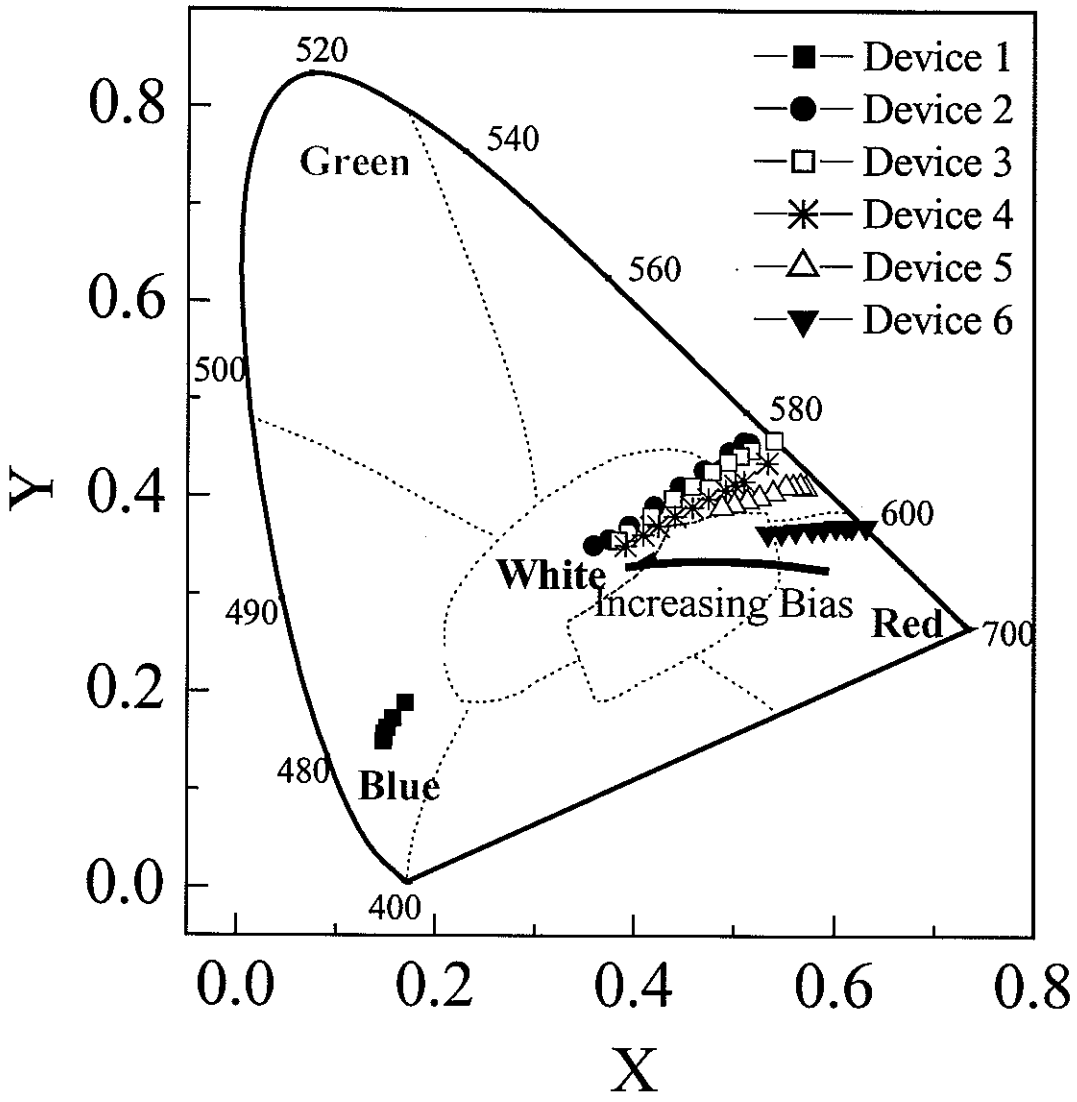

Figure 2. shows the color coordinates of all of the devices at $V \geq 5$ V. As in Device 2, the coordinates of all of the OLEDs blue shifted with increasing V; even the undoped Device 1 exhibited a slight color variation with V which saturated at color coordinates (0.15, 0.15).

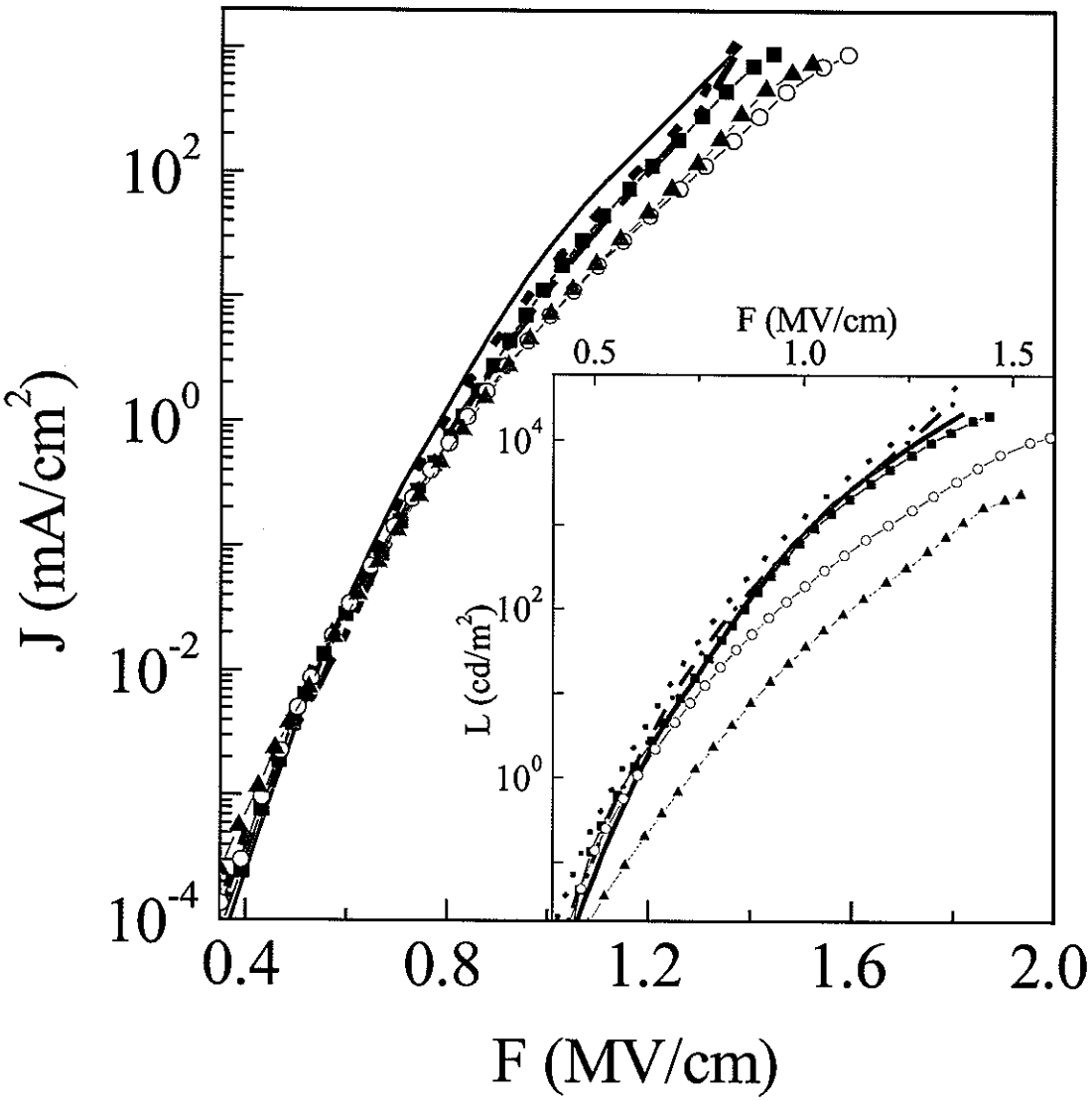

Figure 3. (a) Current density J (a) and (b) luminance L of the OLEDs *vs* average field $F = V/t_{tot}$, where V is the applied voltage and t_{tot} is the total thickness of the organic layers. Inset: L *vs* J.

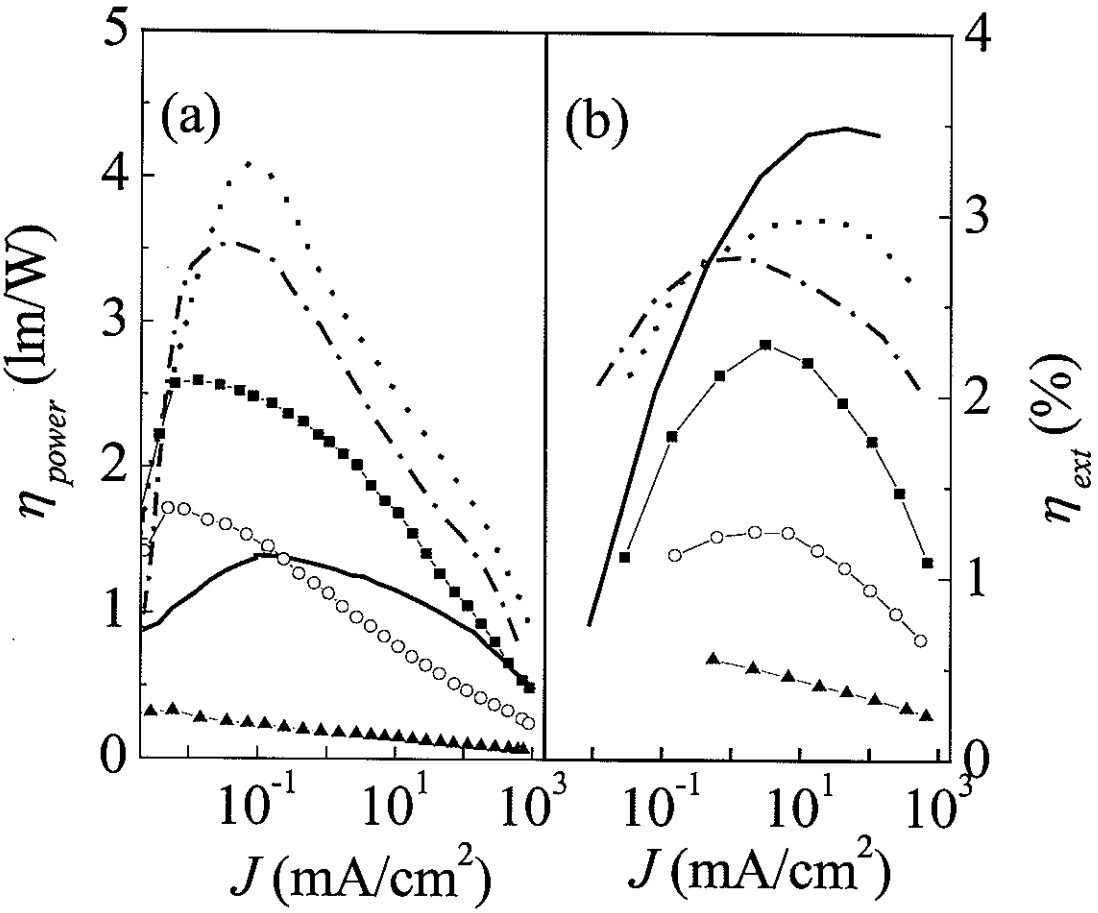

Figure 4. (a) Power efficiencies η_{power} and (b) external quantum efficiencies η_{ext} of the devices vs current density J (The legends are same as in Fig. 3).

0.1 mA/cm^2. η_{power} steadily decreased to 2.4, 2.0, 1.5, 0.6, and 0.08 lm/W at L = 1000 Cd/m^2 for Devices 2–6, respectively. The neat Device 1 exhibited a lower η_{power} = 1.0 lm/W at L = 1000 Cd/m^2 than the slightly doped Device 2, 3, and 4. However, Device 1 actually had the highest η_{ext} = 3.5% at L = 1000 Cd/m^2. The values of η_{ext} were 3.5%, 3.0%, 2.6%, 2.1%, 1.1%, and 0.3% for Devices 1–6 (Table I), respectively, at that brightness. The discrepancy between the behavior of η_{power} and η_{ext} among the devices is clearly due to the photopic response function of the human eye: The response is maximal at $\lambda \sim 555$ nm, and it rapidly decreases as λ decreases; its value at the DPVBi peak at 460 nm is only 6% of its maximum at 555 nm. Although η_{ext} of Device 2 is low relative to Device 1, η_{power} is higher due to the proximity of the DCM2 peak at 570 nm to 555 nm.

η_{ext} decreased systematically with n_{DCM2} and the doped layer thickness due to the concentration quenching and hole trapping processes, which increase with n_{DCM2} . However, relative to DCM1-doped Alq_3 devices, the decrease in η_{ext} with increasing n_{DCM2} was small. Hence, the white color emission exhibited the very high η_{ext} of 2 – 3 % for Devices 2 and 3.

Conclusions

In summary, we have demonstrated very bright WOLEDs with maximum luminance exceeding 50,000 Cd/m^2 and with very high external quantum efficiencies η_{ext} of up to 3 %. Slight doping of 0.5 wt.% DCM2 in α-NPD improved the luminous power efficiency η_{power} almost threefold, while η_{ext} actually decreased from 3.5 % in the undoped devices to 3.0% in the slightly doped device. η_{power} decreased with increasing dopant concentration or increasing dopant layer thickness. The current also decreased with increasing dopant

concentration and doped layer thickness, most likely as a result of the hole traps induced by the higher HOMO level of DCM2 relative to α-NPD, and the consequent reduction in the hole mobility in this layer. The color coordinates of the doped devices evolved well into the white range with increasing bias, i.e., they lacked color saturation.

Acknowledgments

Ames Laboratory is operated by Iowa State University for the U.S. Department of Energy under Contract No. W-7405-ENG-82. This work was supported by the Director for Energy Research, Office of Basic Energy Sciences.

References

[1] C. W. Tang, S. A. Van Slyke, and C. H. Chen, J. Appl. Phys. **65**, 3610 (1989).

[2] R. S. Deshpande, V. Bulovic´, and S. R. Forrest, Appl. Phys. Lett. **75**, 888 (1999).

[3] C. Hosokawa, M. Eida, M. Matsuura, K. Fukuoka, and H. Nakamura, T. Kusumoto, Synth. Met., **91** (1997) 3.

[4] Brian W. D'Andrade, Marc A. Baldo, Chihaya Adachi, Jason Brooks, Mark E. Thompson, and Stephen R. Forrest, Appl. Phys. Lett. **79**, 1045 (2001).

[5] Z. Y. Xie, J. S. Huang, C. N. Li, S. Y. Liu, Y. Wang, Y. Q. Li, and J. C. Shen, Appl. Phys. Lett. **74**, 641 (1999).

[6] P. Destruel, P. Jolinat, R. Clergereaux, and J. Farenc, J. Appl. Phys. **85**, 397 (1999).

[7] C. W. Ko and Y. T. Tao, Appl. Phys.Lett **79**, 4234 (2001).

[8] C.-H. Kim and J. Shinar, Appl. Phys.Lett **80**, 2201 (2002).

[9] C. Hosokawa, H. Higashi, H. Nakamura, and T. Kusumoto, Appl. Phys.Lett. **67**, 3853 (1995).

[10] S. E. Shaheen, G. E. Jabbour, M. M. Morrell, Y. Kawabe, B. Kippelen, N. Peyghambarian, M.-F. Nabor, R. Schlaf, E. A. Mash, and N. R. Armstrong, J. Appl. Phys. **84**, 2324 (1998).

[11] Hubert Spreitzer, Hermann Schenk, Josef Salbeck, Frank Weissoertel, Heike Riel, and Walter Riess, Proc. SPIE Vol. **3797**, 316 (1999).

[12] F. Li, H. Tang, J. Anderegg, and J. Shinar, Appl. Phys. Lett. **70**, 1233 (1997).

[13] F. Li, H. Tang, J. Shinar, O. Resto, and S. Z. Weisz, Appl. Phys. Lett. **70**, 2741 (1997).

[14] L. Zou, V. Savvate'ev, J. Booher, C.-H. Kim, and J. Shinar, Appl. Phys. Lett. **79**, 2282

(2001).

[15] I. G. Hill and A. Kahn, J. Appl. Phys. **86**, 2116 (1999).

[16] E. W. Forsythe, M. A. Abkowitz, Yongli Gao, and C. W. Tang, J. Vac. Sci. Technol. A **18**(4), 1869 (2000).

[17] N. von Malm, J. Steiger, R. Schmechel, and H. von Seggern, J. Appl. Phys. **89**, 5559 (2001).

[18] Yuji Hamada, Hiroshi Kanno, Tsuyoshi Tsujioka, Hisakazu Takahashi, and Tatsuro Usuki, Appl. Phys. Lett. **75**, 1682 (1999).

3. COMBINATORIAL FABRICATION AND STUDY OF DOPED-LAYER-THICKNESS DEPENDENT COLOR EVOLUTION IN BRIGHT SMALL MOLECULAR ORGANIC LIGHT-EMITTING DEVICES

A manuscript submitted to Applied Physics Letters

K. O. Cheon and J. Shinar

Abstract

The behavior of [N,N'-diphenyl-N,N'-bis(1-naphthylphenyl)-1,1'-biphenyl-4,4'-diamine (α-NPD)]/[5 ± 0.6 wt.% [2-methyl-6-[2-(2,3,6,7-tetrahydro-1H,5H-benzo[i,j]quinolizin-9-yl) ethenyl]-4H-pyran-4-ylidene]propane-dinitrile (DCM2)-doped α-NPD]/[4,4'-bis(2,2'-diphenyl-vinyl)-1,1'-biphenyl (DPVBi)] organic light-emitting devices is described. The color of the devices shifts from blue to red as the thickness of the doped layer increases from 0 to 35 Å. The (nominal) 2 Å-thick doped layer device exhibited the highest brightness $L \sim 120$ Cd/m^2 and external quantum efficiency $\eta_{ext} \sim 4.4$ % at a current density of 1 mA/cm^2.

Introduction

Color modification in thermal vacuum evaporated small molecular organic light-emitting devices (OLEDs) has attracted strong attention due to the potential and actual applications of such OLEDs for flat panel displays [1] and general lighting [2] applications. Indeed, it has been relatively easy to control the emission color of these devices. One of the well-known

methods is the guest-host (G-H) or molecular doped approach, where both the doping concentration [1,3-5] and applied bias [5,6] affect the emission spectrum. The guest emission spectra are shifted by the doping concentration [3-5] and the relative intensity of guest and host emission vary with applied bias [5,6]. Yet control of the doping concentration is problematic due to instabilities in the fabrication procedure. In contrast, color tuning via changes in the thickness of the doped layer may provide a facile fabrication process for the vacuum evaporated devices. This letter demonstrates this new approach and considers the physical processes which control it.

In the typical G-H film, the guest molecule, with a relatively low gap between the highest occupied molecular orbital (HOMO) and lowest unoccupied molecular orbital (LUMO), is doped into the higher HOMO-LUMO gap host molecule. If the absorption spectrum of the guest partially or fully overlaps the emission spectrum of the host, then the excitons of the host are transferred nonradiatively to the guest fluorophores [7,8]. Thus the dopant molecule emits light with its own spectrum. However, trap emission is another possible emission mechanism: Since either the HOMO or the LUMO level of the guest is in the host HOMO-LUMO gap, the guest molecule traps charge carriers [9], becoming a trap emission center [10].

The guest emission energy may change considerably with doping concentration c_d. For example, in 0.5 wt.% DCM2 in α-NPD the emission peak is at 2.18 eV (570 nm), but in 5 wt.% it is 1.96 eV (632 nm) [5]. This solid-state solvation effect (SSSE) [1,3] red shift is explained by dipole-dipole interaction between the excited guest molecules and surrounding dipoles: With increasing polarization of the host by increased doping with the highly polar DCM2 molecule, the DCM2 emission itself red-shifts [3]. In this letter, we show that the

doping thickness t_d, rather than c_d, may affect the host polarization, if t_d is less than the dipole-dipole interaction range.

Device structures and measurement methods

The multilayer devices were deposited at 0.5 - 2 Å/sec on aquaregia-treated 2"×2" ITO substrates [11] by conventional thermal evaporation in a vacuum chamber (<10^{-6} Torr) installed inside an Ar-filled glove box; the oxygen and water levels were below 1 ppm. A 5 nm thick copper phthalocyanine (CuPc) layer was used to improve hole injection from ITO. It was followed by a 38 nm thick α-NPD hole transport layer. For color tuning, DCM2 and α-NPD were co-deposited after the neat α-NPD layer; their depositions rates corresponded to $c_d = 5 \pm 0.6$ wt.% DCM2 in α-NPD. The sliding shutter technique, which has 21 mechanical steps in 2", was used to vary the thickness of the doped layer [12]. The shutter was completely closed during the stabilization of the DCM2 and α-NPD deposition rates. After

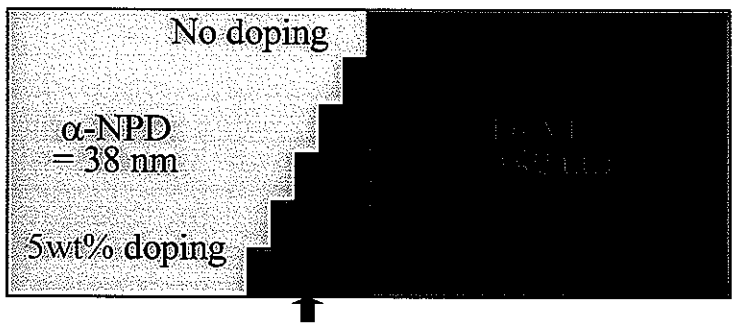

Figure 1. Schematic device diagram of the DCM2 doped α-NPD layer. Nominal doping thickness t_d varies from 0 to 35 Å.

their stabilization, the shutter was opened except for the first 4 columns (which resulted in undoped devices), and the shutter was kept moving every 2 columns, resulting in nominal doped layer thicknesses t_d = 1, 2, 3, 4, 6, 10, 20, and 35 Å (see Fig. 1). It should be noted that the gap between the substrate and shutter was ~2 mm, so the shadow effect may have affected the real doping thickness. However, the variation in t_d was still systematic. To generate the host (i.e., donor) fluorescence [8], a 40 nm thick 4,4'-bis(2,2'-diphenylvinyl)-1,1'-biphenyl (DPVBi) blue emitting layer was deposited, and followed by a 10 nm thick Alq_3 electron transport layer. Finally, a 1 nm thick CsF layer was evaporated to improve the electron injection from the 150 nm Al cathode. The Al was deposited through a 2"×2" mask containing 21×21 hole pixels, each ~1.5 mm in diameter. The maximum EL of some of the pixels in this array exceeded 50,000 cd/m^2 [5], as measured by a Minolta LS110 luminance meter and/or a Hamamatsu 3456 photomultiplier tube (PMT). The EL spectra were measured using an Ocean Optics CHEM2000 integrated spectrometer.

Experimental results and discussions

Figure 2 shows the peak emission energy E_{max} of the DCM2 emission versus t_d; the inset shows the EL spectra for t_d = 1 Å (solid squares), 2 Å (open circles), and 35 Å (open triangles). For t_d < 10 Å, the thickness is obviously a nominal thickness only, since a uniform monolayer is ~6 Å thick. E_{max} of a device with t_d = 100 Å was adopted from previous work [5]. All of the data in Fig. 2 were taken at an applied bias V_{app} = 10 V. To determine the precise E_{max}, the orange-red and blue emission bands were deconvoluted into two Gaussians. The actual blue emission was negligible for $t_d \geq 2$ Å.

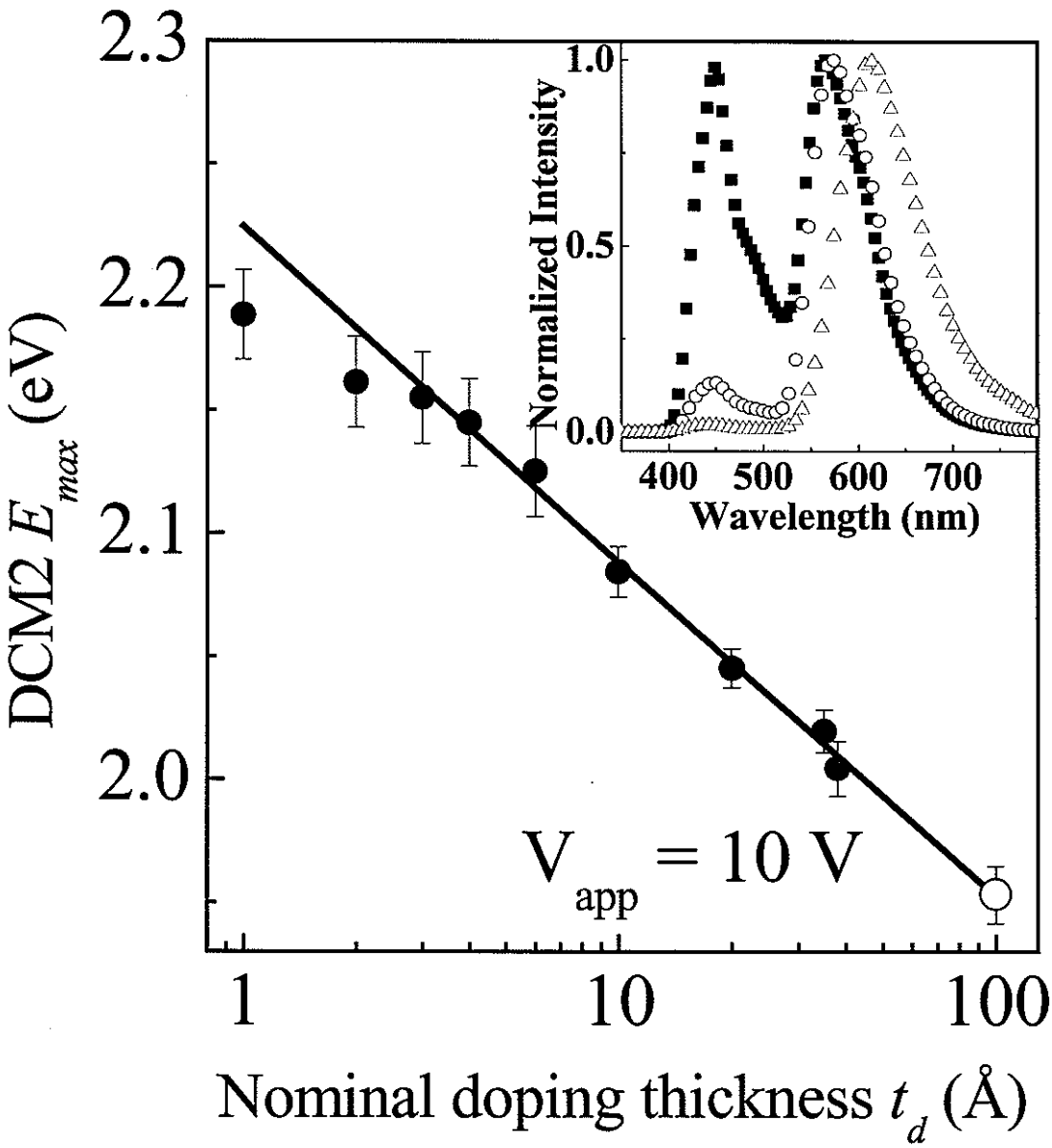

Figure 2. Peak emission energy of DCM2 vs. $log(t_d)$ for the fixed doping level 5 ± 0.6 wt.%. Inset: EL spectra for t_d = 1 Å (solid squares), 2 Å (open circles), and 35 Å (open triangles). The emission peaks at ~460 and ~600 nm are due to DPVBi and DCM2, respectively.

Figure 2 shows that E_{max} red-shifts from 2.15 eV (575 nm) for t_d = 1 Å to 2.0 eV (620 nm) for t_d = 35 Å. The circles are the experimental values, and the linear line is the logarithmic fit to the data. The error bars represent the asymmetry and the ambiguity of the peaks of the spectra due to the vibronic modes.

Figure 3 shows the brightness L (Cd/m^2), power efficiency η_{power} (lm/W) and external quantum efficiency η_{ext} (%) (estimated from L and spectrum analysis [13]) versus t_d at a constant current density J = 1 mA/cm^2 (solid squares) and 10 mA/cm^2 (open circles). Initially, L increases rapidly with t_d, peaking at t_d = 2 Å; L_{max} = 120 Cd/m^2 for J = 1 mA/cm^2, and 1050 Cd/m^2 for J = 10 mA/cm^2. Beyond the maximum, L decreases gradually with increasing t_d. The efficiencies η_{power} and η_{ext} behave similarly, but they are higher at the lower current density J = 1 mA/cm^2. At this J, $\eta_{ext} \approx 3\%$ for the undoped sample; it increases to a maximum of 4.4% for t_d = 2 Å, and decreases to 1.4 % for t_d = 35 Å.

Figure 4 shows the evolution of the color coordinates of the devices with t_d at V_{app} = 8 V and 10 V. The coordinates start from blue, cross the white region, and quickly approach orange and red. At V_{app} = 10 V the color of the undoped device is blue [(x, y) = (0.15, 0.15)], for the t_d = 1 Å device it is a near-ideal white [(x, y) = (0.35, 0.33)], and for the t_d = 35 Å it is red [(x, y) = (0.61, 0.37)].

Figure 5 shows an array of pixels with different t_d on the 2"×2" substrate. All of the pixels were turned on at the same time, with V_{app} = 8 V. There was no intentional DCM2 doping in the first two columns, t_d was 1 Å in the third column, and beyond that column, t_d increased nonlinearly to 35 Å in the last columns.

The t_d-dependence of both E_{max} (Fig. 2) and the efficiencies (Figs. 3(b), (c)) are very similar to their doping concentration (c_d)-dependence described previously [1,3-5]: First, the

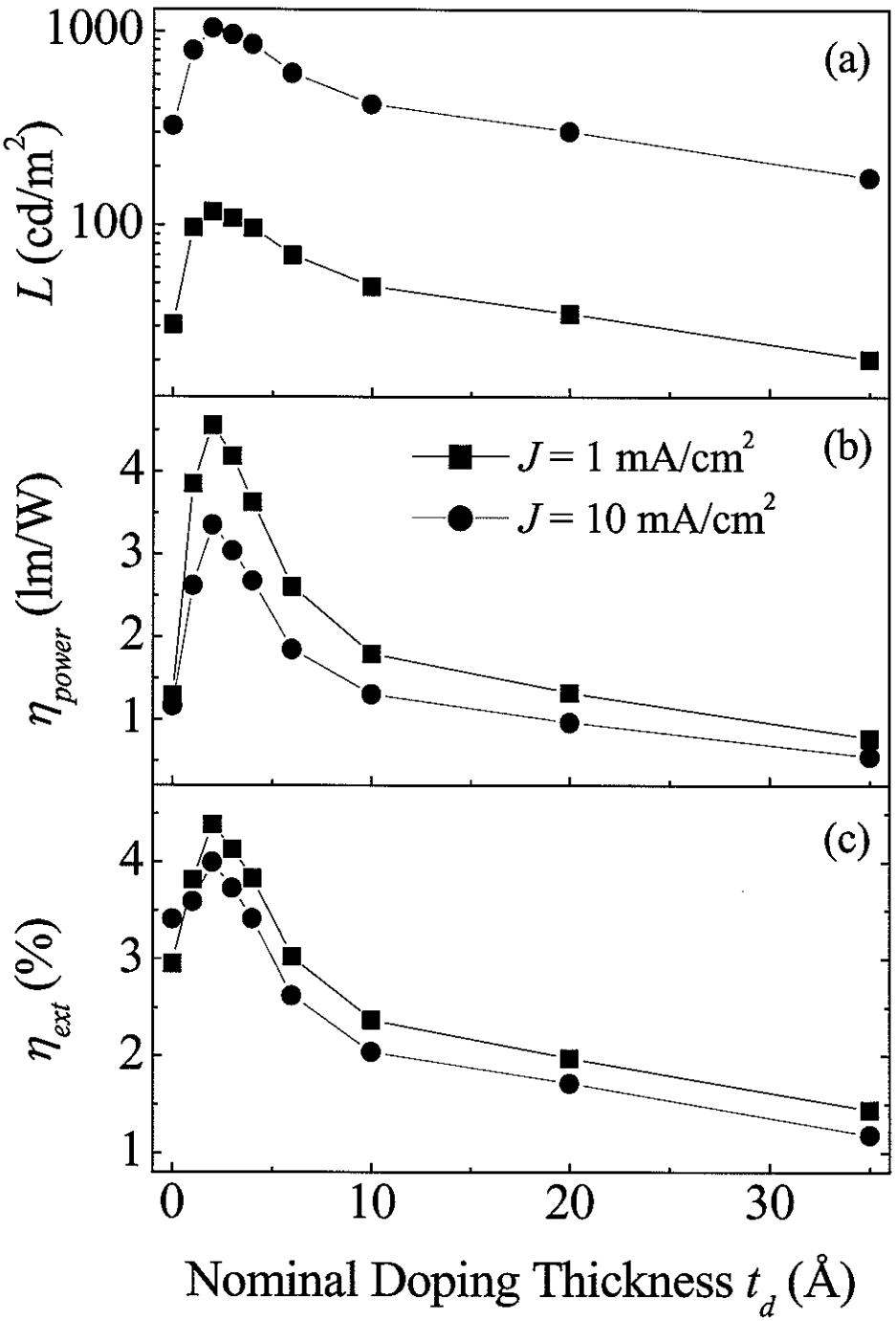

Figure 3. The brightness L (Cd/m^2), power efficiency η_{power} (lm/W), and external quantum efficiency η_{ext} (%) for different DCM2-doped layer thicknesses, at $J = 1$ and 10 mA/cm^2.

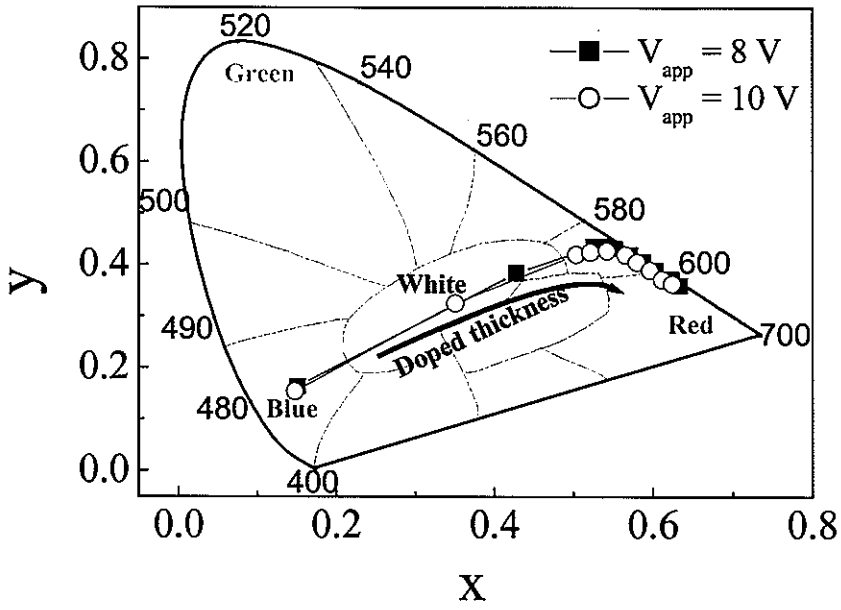

Figure 4. Doping-thickness-dependence of the color coordinates for V_{app} = 8 V, and 10 V.

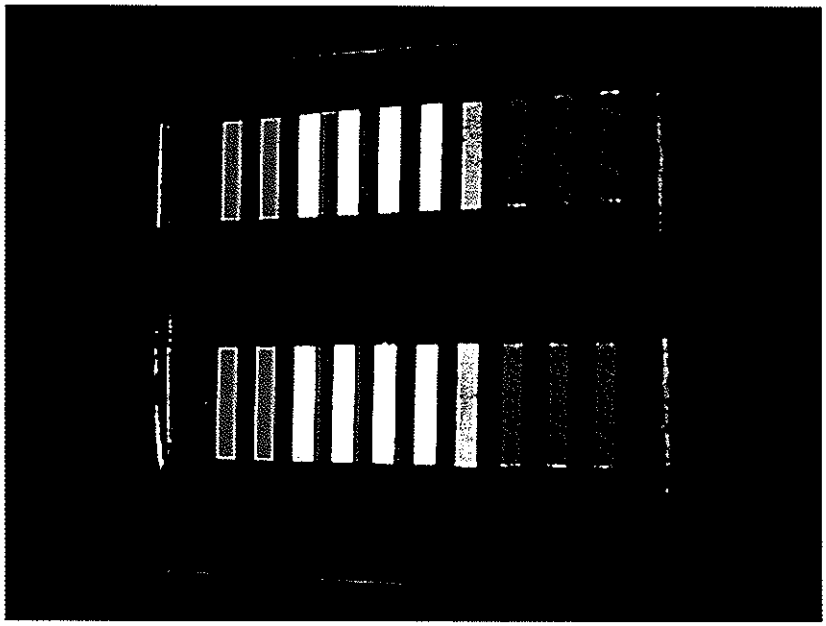

Figure 5. Real color evolution of OLEDs with varying DCM2-doped-layer thickness at V_{app} = 8 V.

logarithmic dependence of E_{max} on t_d is similar to its dependence on c_d in DCM2-doped Alq_3 [3], where this behavior was explained by local ordering of polar molecules, with a maximum domain radius $R_c \sim 110$ Å. The typical intermolecular spacing is known to be ~ 8 Å in amorphous molecular thin films [3,4], so c_d is directly proportional to t_d for $t_d \leq 10$ Å. Thus the dependence of E_{max} on t_d and c_d should be the same for $t_d \leq 10$ Å. For $t_d > 10$ Å, E_{max} should become independent of t_d if a fluorophore interacts only with its nearest neighbors, because the number of nearest neighbor DCM2 molecules is determined by c_d. Yet the behavior of E_{max} in Fig. 2 shows that its logarithmic dependence on t_d is still effective up to at least 100 Å. This implies that a DCM2 fluorophore can interact by the dipole-dipole interaction with remote DCM2 molecules which are 100 Å away. Thus the dipole-dipole interaction range is ≥ 100 Å, similar to the domain size $R_c \sim 110$ Å resulting from the local ordering model of DCM2 in Alq_3 [3]. Within the dipole-dipole interaction range or in an ordered domain, all of the DCM2 molecules interact collectively. For $t_d \leq R_c$, the total number of DCM2 molecules in a domain can be controlled either by c_d or by t_d. Hence, for $t_d \leq R_c$, the logarithmic dependence of E_{max} on t_d should be, and is, the same as its dependence on c_d.

Second, for 4-(dicyanomethylene)-2-methyl-6-(p-dimethyl aminostyryl)-4H-pyran (DCM1) in Alq_3, the PL [4,14] and EL [10,14] efficiencies were found to be maximal at low doping levels $0.2 \leq c_d \leq 3$ mol%. The t_d-dependence of the efficiencies of DCM2 in this work (Fig. 3(b), 3(c)) is similar: it rapidly rises to the maximum, and then monotonically decreases with t_d up to 100 Å; in the 100 Å device, $\eta_{ext} \approx 0.5$ % [5] at $J = 1$ mA/cm^2 (not shown in Fig. 3). Thus the efficiency is affected by doping up to at least $t_d \sim 100$ Å, and the explanation for

the t_d-dependence of the energy shift can apply to the efficiency, and both are similar to the c_d-dependence for $t_d \leq R_c$.

Conclusions

In conclusion, the emission color of [α-NPD]/[5 wt.% DCM2 in α-NPD]/[DPVBi] OLEDs is found to vary from blue to red as the doped layer thickness increases from 0 to 35 Å, due largely to the effect of the thickness on the guest emission spectrum. This behavior is due to the dipole-dipole interaction among the DCM2 molecules, whose range is greater than 100 Å. Hence the doped layer thickness t_d-dependence of the emission color and efficiency is similar to the doping concentration c_d dependence. The t_d = 2 Å nominal doping thickness device exhibited the highest performances in brightness (L~ 120 cd/m^2) and in efficiency (η_{ext} ~ 4.4 %) at J = 1 mA/cm^2.

Acknowledgements

This manuscript was authored by Iowa State University of Science and Technology under Contract No. W-7405-ENG-82 with the U.S. Department of Energy.

References

[1] V. Bulović, A. Shoustikov, M. A. Baldo, E. Bose, V.G. Kozlov, M. E. Thompson, and S. R. Forrest, Chem. Phys. Lett. **287**, 455 (1998).

[2] A. R. Duggal, J. J. Shiang, C. M. Heller, and D. F. Foust, Appl. Phys. Lett. **80**, 3470 (2002).

[3] M. A. Baldo, Z. G. Soos, and S. R. Forrest, Chem. Phys. Lett. **347**, 297 (2001).

[4] G. Y. Zhong, J. He, S. T. Zhang, Z. Xu, Z. H. Xiong, H. Z. Shi, X. M. Ding, W. Huang, and X. Y. Hou, Appl. Phys. Lett. **80**, 4846 (2002).

[5] K. O. Cheon and J. Shinar, Appl. Phys. Lett. **81**, 1783 (2002).

[6] J. Kalinowski, P. Di Marco, V. Fattori, L. Giulietti, and M. Cocchi, J. Appl. Phys. **83**, 4242 (1998).

[7] M. Pope and C. E. Swenberg, Electronic Processes in Organic Crystals (Oxford University Press, Oxford, 1982).

[8] K. O. Cheon and J. Shinar, to be submitted

[9] N. von Malm, J. Steiger, R. Schmechel, and H. von Seggern, J. Appl. Phys. **89**, 5559 (2001).

[10] J. Littman and P. Martic, J. Appl. Phys. **72**, 1957 (1992).

[11] F. Li, H. Tang, J. Shinar, O. Resto, and S. Z. Weisz, Appl. Phys. Lett. **70**, 2741 (1997).

[12] L. Zou, V. Savvate'ev, J. Booher, C.-H. Kim, and J. Shinar, Appl. Phys. Lett. **79**, 2282 (2001).

[13] D. O'Brien, A. Bleyer, D. G. Lidzey, D. D. C. Bradley, and T. Tsutsui, J. Appl. Phys. **82**, 2662 (1997).

[14] J. Kalinowski, L. C. Picciolo, H. Murata, and Z. H. Kafafi, J. Appl. Phys. **89**, 1866 (2001).

4. FÖRSTER ENERGY TRANSFER AND THE EMISSION ZONE IN SELECTIVE DOPED ORGANIC LIGHT EMITTING DEVICES

K. O. Cheon and J. Shinar

A manuscript prepared for submission to Applied Physics Letters

Abstract

Energy transfer in highly efficient doped organic light-emitting devices (OLEDs) is described and discussed. The OLEDs include a hole transport layer of N,N'-diphenyl-N,N'-bis(1-naphthylphenyl)-1,1'-biphenyl-4,4'-diamine (α-NPD) and the electron transport and emitting layer 4,4'-bis(2,2'-diphenylvinyl)-1,1'-biphenyl (DPVBi). A region of the α-NPD layer adjacent to the interface with the DPVBi layer was doped with the red dye [2-methyl-6-[2-(2,3,6,7-tetrahydro-1H,5H-benzo[i,j]quinolizin-9-yl)ethenyl]-4H-pyran-4-ylidene]propane-dinitrile (DCM2). By comparing the emission from the DCM2 with that from DPVBi, the energy transfer probability and its dependence on the applied field was determined. The Förster energy transfer radius in this device was determined to be ~30 to ~40 Å.

Introduction

Molecularly doped guest-host (G-H) blends have recently been exploited to improve the efficiency [1,2] or modify the emission color [1,3,4] of organic light emitting devices (OLEDs). The doped guest emission is usually due to energy transfer from the host molecules [2-4], and the energy transfer rate depends on the overlap between the host

emission and guest absorption spectra [5]. In most of the efficient G-H OLEDs the highest occupied molecular orbital (HOMO) and lowest unoccupied molecular orbital (LUMO) levels of the guest are inside the host HOMO-LUMO gap. This situation satisfies the spectral overlap condition if the Stokes shifts between the absorption and emission spectra of the host and guest are not too large. However, since the guest HOMO and LUMO levels are inside the host HOMO-LUMO gap, they generate carrier trap states, which reduce the current flowing through the devices [6,7].

In most of the efficient G-H OLEDs the overall emission color varies with bias because the ratio of guest-to-host emission is bias-dependent and generally decreases with applied bias [7,8]. In case of energy transfer the decrease in ratio that is observed can be understood by electric field quenching. Apparently the field-induced quenching occurs while the host exciton energy is transferred to the guest molecule. In general, due to field-induced quenching, efficient OLED operation is limited to average electric fields below ~2 MV/cm. Indeed, photoluminescence (PL) measurements on the blend of poly (phenyl-p-phenylene vinylene) (PPPV) and bisphenol-A-polycarbonate (PC) [9] demonstrated that the PL intensity was quenched by ~30% at 2 MV/cm. However, in some efficient devices the strong evolution of the color with bias cannot be explained by electric field quenching [7]. To study the color evolution and Förster energy transfer mechanism in such OLEDs, the selective doping method [10] was used to dope very efficient blue OLEDs based on the hole transporting material N,N'-diphenyl-N,N'-bis(1-naphthylphenyl)-1,1'-biphenyl-4,4'-diamine (α-NPD) and the electron transporting and blue-emitting material 4,4'-bis(2,2'-diphenylvinyl)-1,1'-biphenyl (DPVBi) [11].

Device structures and measurements

The OLED fabrication procedure was described elsewhere [7]. A 5 nm-thick copper phthalocyanine (CuPc) layer was deposited directly above the indium tin oxide anode, followed by a 40 nm-thick α-NPD layer. Then a 1 nm thick layer of the red-emitting [2-methyl-6-[2-(2,3,6,7-tetrahydro-1H,5H-benzo[i,j]quinolizin-9-yl)ethenyl]-4H-pyran-4-ylidene]propane-dinitrile (DCM2) dye was co-deposited with the host α-NPD. The nominal doping level of DCM2 in α-NPD was 1 wt.%, which corresponds to 1.6 mol%. This doped layer was followed by another pure α-NPD layer of varying thickness D = 0, 1, 2, and 5 nm (Fig. 1). This layer was followed by a 40 nm thick layer of blue-emitting DPVBi, a 10 nm thick electron transporting layer of tris(8-hydroxyquinoline) Al (Alq_3), a 1 nm thick CsF buffer layer, and a 150 nm thick Al cathode; the OLED pixel diameter was ~1.5 mm. To minimize batch-to-batch variations among the OLEDs, all of the devices were made on the

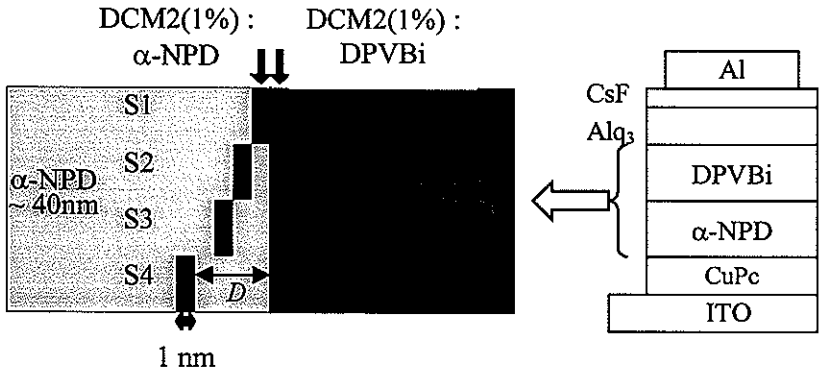

Figure 1. Structures of the OLEDs. The nominal thickness D of the undoped α-NPD "gap" layer is 0, 1, 2, and 5 nm for devices S1, S2, S3, and S4 respectively. The DCM2 is also doped into the DPVBi layer with the same method used for DCM2 doping in the α-NPD layer.

same substrate during the same deposition run using a sliding shutter technique [7]. The emission zone of small molecular devices could be identified by thin, selective doping method [10]. To identity the emission zone very thin DCM2 doped layers were also inserted in the DPVBi layer (see Fig. 1). The brightness was determined using a Minolta LS110 luminance meter and/or Hamamatsu 3456 photomultiplier tube, while the electroluminescence (EL) spectra were obtained using an Ocean Optics CHEM2000 integrated spectrometer.

In these (40 nm α-NPD)/(1 nm DCM2:α-NPD)/(*D* nm α-NPD)/(40 nm DPBVi)/(10 nm Alq_3) OLEDs, electron-hole recombination occurs in the DPVBi layer. Hence emission from the guest is due to resonant Förster energy transfer from DPVBi to the DCM2 molecules [7], and information on this energy transfer can be deduced from systematic variations in the distance *D*.

Theory

In the Förster process, an exciton on the donor induces a dipole in the acceptor molecule. The inducing donor field can interact with the induced acceptor dipole [5]. The interaction is proportional to D^{-6} and to the overlap integral R_0^6 of the host emission and guest absorption spectra. The predicted transfer probability from host to guest P_{HG}^{Q} can then be expressed as [4]

$$P_{HG}^{Q} = \frac{\alpha \cdot Q}{1 + \alpha \cdot Q} \tag{1}$$

where Q is the doping concentration and $\alpha \equiv (R_0 / D)^6$. On the other hand, the actual transfer probability P_{HG}^{η} can be estimated from the number of photons emitted by the host N_H and by

the guest N_G as follows [4]. N_G is proportional to P_{HG}^{η}, the guest PL quantum yield η_G^{PL}, and the total number of singlet excitons N_{tot}^{ex} generated in the host molecules, *i.e.*,

$$N_G \propto \eta_G^{PL} \cdot P_{HG}^{\eta} \cdot N_{tot}^{ex} \tag{2}$$

Similarly, for the host emission,

$$N_H \propto \eta_H^{PL} \cdot \left(1 - P_{HG}^{\eta}\right) \cdot N_{tot}^{ex} \tag{3}$$

If the outcoupling efficiency ξ is the same for guest and host emission, then the proportionality constant in Eqs. (2) and (3) are the same and the equations yield

$$P_{HG}^{\eta} = \frac{\eta_H^{PL}}{\left(N_H / N_G\right) \cdot \eta_G^{PL} + \eta_H^{PL}} \tag{4}$$

The measurements described below yield P_{HG}^{η}, and comparison with Eq. (1) then yields the Förster energy transfer radius R_0.

Experimental results and discussions

Figure 2 shows the EL spectra of device S2 at V = 7, 10, and 14 V. The 460 nm band is due to DPVBi [7]. The 570 nm band, due to the DCM2 dopant, depends on the doping concentration [12]. At low voltage the DPVBi emission is barely noticeable, but its intensity increases rapidly with increasing voltage and it approaches the DCM2 intensity at 14 V; the other devices behave similarly.

The host/guest emission intensity ratio N_H/N_G of device S2 is analyzed in the inset of Fig. 2. To calculate N_H/N_G, the spectra were converted to energy scale (eV) and deconvoluted to two Gaussians; at low bias (V < 5 V), N_H/N_G was estimated by linear and exponential extrapolation based on higher voltage data. In determining the average field E in the device,

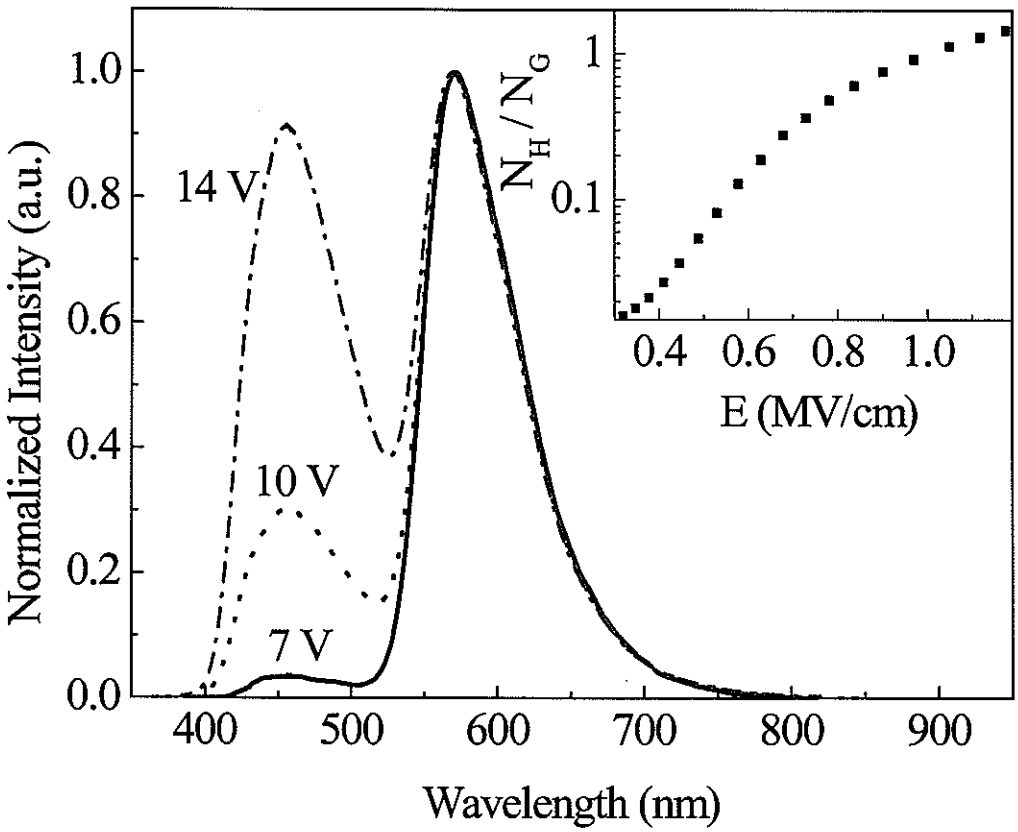

Figure 2. Spectral response of S2 for different applied voltages. Inset : The ratio of photons emitted by the host to photons emitted by the guest.

the built-in potential of $V_{bi} = 2.1$ V [13] was subtracted from V. As clearly seen, N_H/N_G increases dramatically with V, from ~0.015 at 0.3 MV/cm to ~1.5 at 1.2 MV/cm.

Figure 3 shows the external quantum efficiency η_{ext} of device S2 (solid line), separate host and guest efficiencies ($\eta_{ext,H}$ and $\eta_{ext,G}$, respectively), and η_{ext} of the undoped device (dashed line) vs E. The maximum efficiencies $\eta_{ext,max}$ are ~4% for device S1 (not shown) and ~ 3.5% for S2, which are similar to $\eta_{ext,max}$ ~ 3.5% of the undoped device. With increasing field $\eta_{ext,H}$ increases but $\eta_{ext,G}$ decreases rapidly. The latter is partially due to electric field quenching, which can quench the excitons during the energy transfer from DPVBi to DCM2 fluorophores. The relative change of $\eta_{ext,G}$ vs. $\eta_{ext,H}$ is higher than that expected from electric field quenching by a few tenth of a percent.

In small molecular OLEDs, it is generally believed that 25% of the excitons are singlets, and η^{PL} of these decay radiatively. In devices in which the electron and hole injection is balanced, η^{PL} can be estimated from the outcoupling efficiency $\xi \approx 1/n^2$ (where n is the index of refraction of the ITO/glass) [14] and η_{ext}. In the undoped α-NPD/DPVBi device, η_{ext} ≈ 3.5% yields $\eta^{PL}_{DPVBi} \sim 45\%$. For DCM2, assuming 100% energy transfer from DPVBi in device S1 at $\eta_{ext,max}$, we obtain $\eta^{PL}_{DCM2} \sim 52\%$. This latter value is in striking agreement with the 53% PL quantum yield of DCM2 in CBP [2].

Given $\eta^{PL}_{DCM2} \sim 52\%$ and $\eta^{PL}_{DPVBi} \sim 45\%$, and assuming that the DCM2 molecules are excited only by Förster energy transfer from the host, Eq. (4) now yields P_{HG} vs. E (see Fig. 4(a)). As clearly seen, P_{HG} is not constant. In devices S1 and S2 it is close to 1 below 0.6 MV/cm, but decreases at higher fields. In devices S3 and S4, it decreases at low fields and

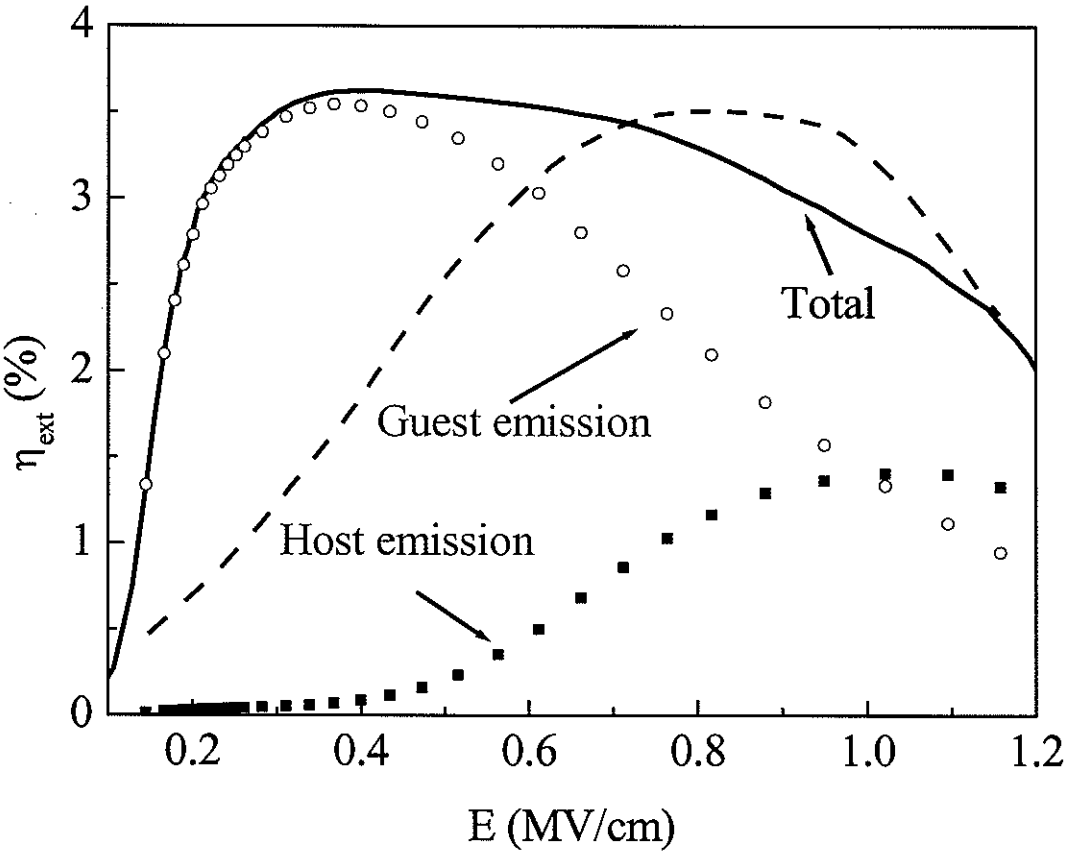

Figure 3. External quantum efficiencies η_{ext} of device S2, and separated efficiencies of host and guest emission. The dashed line is the efficiency of pure undoped α-NPD/DPVBi.

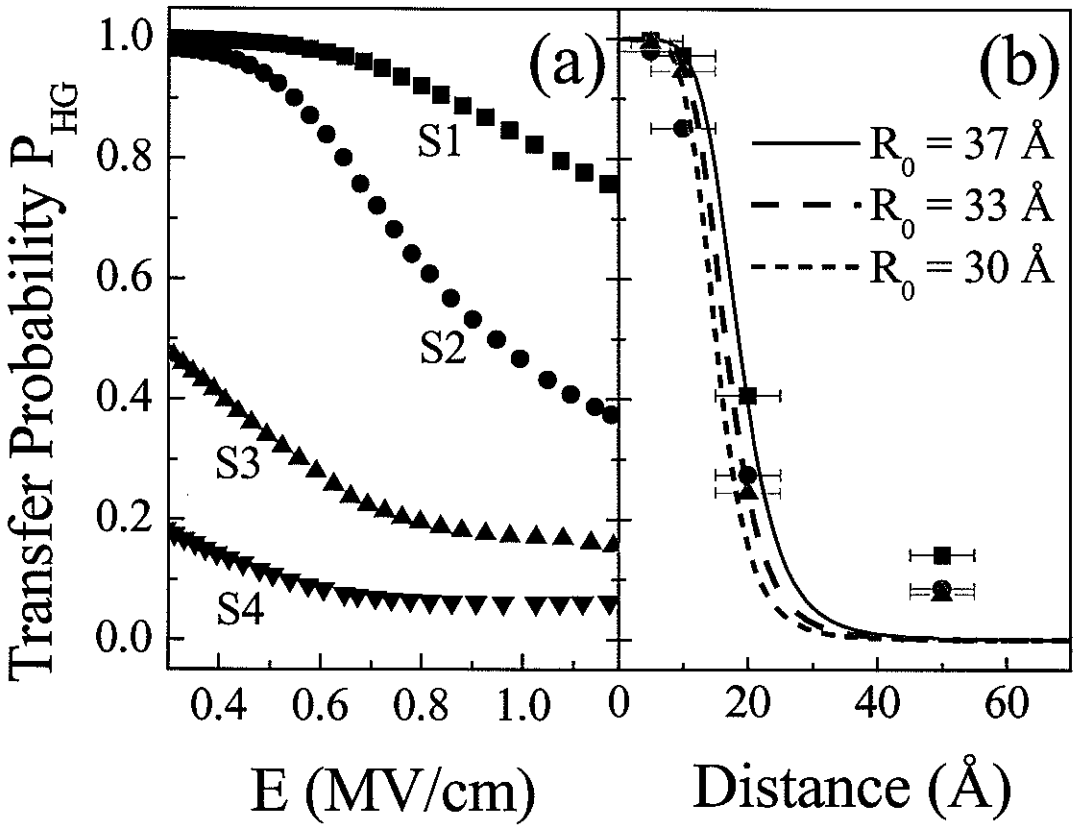

Figure 4. Energy transfer probability P_{HG} : (a) electric field dependence, and (b) distance dependence.

levels off at high fields. Possible explanations for its behavior include trap emission and quenching by trapped charges and the applied field. At low field, trap emission is more significant, since DCM2 is known to be a hole trap in α-NPD [7] so the trapped-charge density increases with increasing current.

The efficiency η_{ext} of the undoped device peaks at 0.8 MV/cm (Fig. 3), but η_{ext} of the doped device S2 peaks at 0.4 MV/cm. This difference is partially due to direct trapped charge from the guest. With increasing field the recombination zone gradually narrows [8] and moves to the α-NPD/DPVBi interface, so at higher field trap emission contributes less to the overall guest emission. At the same time, due to the increased hole injection more DCM2 trap-sites the inside α-NPD layer become filled by holes, but not enough electrons are supplied to the DCM2 trap-sites due to the electron energy barrier at α-NPD/DPVBi interface. Since energy transfer by dipole-dipole interaction to the ionized guest is not possible, P_{HG} decreases due to the reduced number of available neutral guest fluorophores.

Figure 4(b) shows how different values of R_0 fit the behavior of P_{HG} (solid squares are P_{HG} at 0.4 MV/cm, solid circles are P_{HG} at 0.6 MV/cm; the error bars are due to the uncertainty in D). The minimum G-H distance of device S1 should be farther than the molecular distance between G and H at contact (~ 5 Å) [15] even though there is no gap between the doped layer and host emitting DPVBi layer. For other devices, instead of the distance to the center of the doped layer, the nominal gap distances D are used due to the D^{-6}-dependence of the energy transfer.

The lines in Fig. 4(b) are calculated from Eq. (1) using R_0 = 37 Å for 0.4 MV/cm (solid line), and R_0 = 30 Å for 0.6 MV/cm (dashed line) to fit the values of P_{HG} from Fig. 4(a). These values of R_0 are in good agreement with a typical Förster energy transfer radius of 30 –

40 Å [12]. The substantial efficiency of the pure α-NPD/DPVBi device is about a half of the DCM2 efficiency of device S2 at 0.4 MV/cm (see Fig. 3). Thus it appears that at 0.4 MV/cm, 50% of the guest emission does not occur by energy transfer from the host. Consequently, the solid triangles in Fig. 4(b) were obtained by assuming that 50% of DCM2 emission is due to carriers trapped by DCM2, and the values yield R_0 = 33 Å. At higher fields, P_{HG} deviates considerably from the low-field value due to other effects, so the analysis of its behavior is more complex.

Figure 5 shows P_{HG}, or, equivalently, the DCM2 emission probability (circles) in the recombination zone. Basically, the DCM2 emission in α-NPD is caused by the Förster energy transfer process discussed above. However, the DCM2 emission probability in DCM2 doped DPVBi layer could not be fitted by the straightforward Förster process, so the dashed line on the DPVBi side is only a guide to the eye. The unbalanced DCM2 emission probability for both sides can be clearly understood by the original exciton distribution profile of undoped α-NPD/DPVBi device (square-line); exciton distribution was calculated using the parameters given in Table 1. The exciton distribution of the undoped sample has a relatively sharp edge at the α-NPD side. This implies that the donor-acceptor distance D is

Table 1. Parameters for the numerical simulation of the singlet exciton distribution. The most important parameters are the mobilities and energy levels (see Chapter 1).

	μ_{e0} (cm^2/Vs)	μ_{h0} (cm^2/Vs)	$F_0^{-1/2}$ $(cm/V)^{1/2}$	E_{LUMO} (eV)	E_{HOMO} (eV)
α-NPD	10^{-6}	10^{-4}	1.5×10^{-3}	2.3	5.4
DPVBi	5×10^{-7}	5×10^{-9}	9×10^{-3}	2.8	5.9

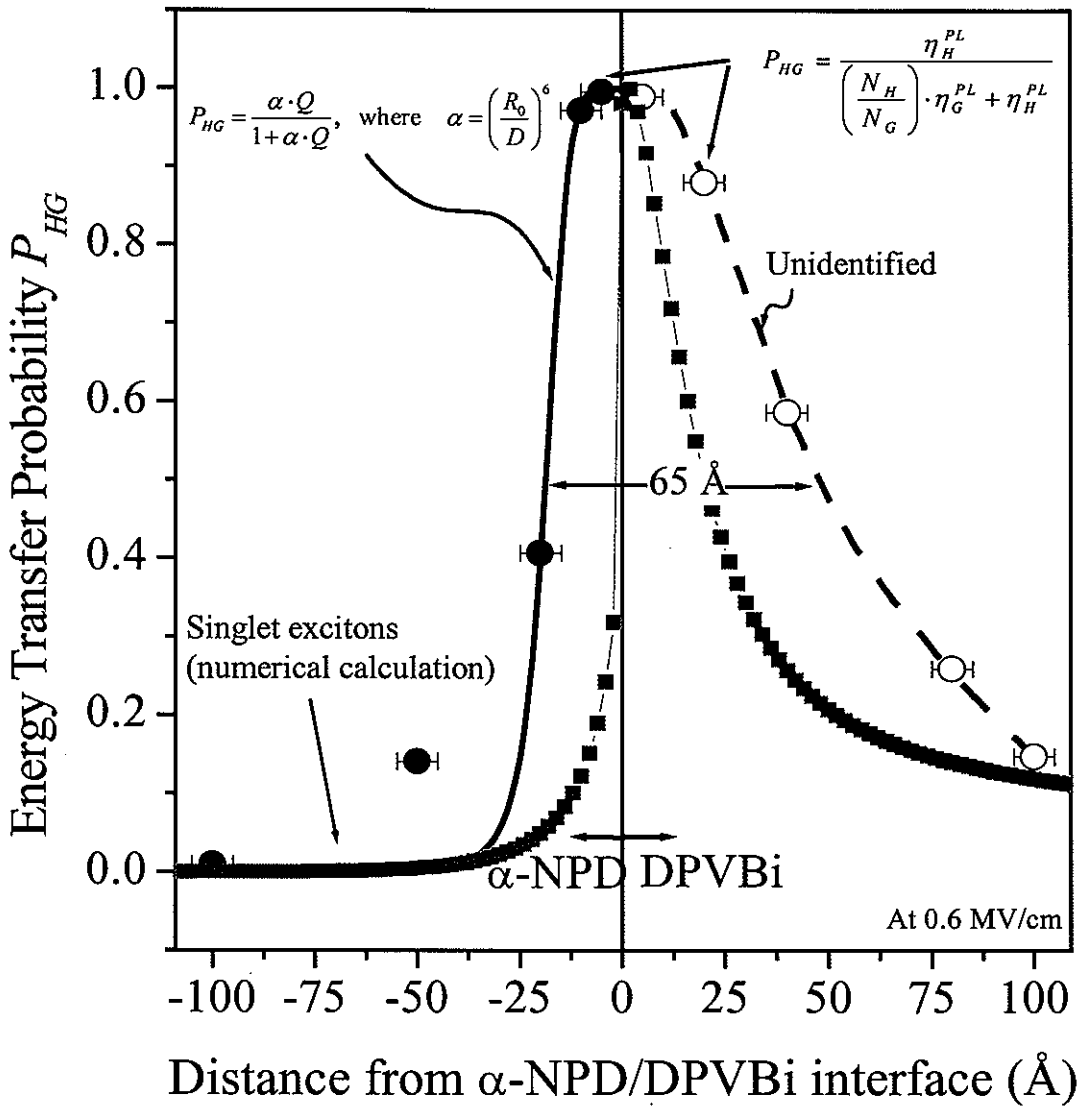

Figure 5. Energy transfer probability P_{HG} in the recombination zone of α-NPD/DPVBi devices. Circles are experimentally estimated from the spectral analysis of the DCM2 doped devices for different distances D at a electric field 0.6 MV/cm. For α-NPD side, the experimental values are compared with the calculated Förster energy transfer process, with R_0 = 30 Å (solid line). The dashed line on the DPVBi side is a guide to the eye. The square-line is the exciton distribution calculated from the numerical simulation of undoped α-NPD/DPVBi devices.

well defined for energy transfer from the DPVBi donor to an acceptor in the α-NPD side. However, due to the relatively broad donor exciton distribution in the DPVBi layer, with about 20 Å width at half-maximum (see Fig. 5), the donor-acceptor distance cannot be defined by single value D. That is why the DCM2 emission probability in DPVBi does not follow the straightforward Förster process.

If we define the emission zone width as the width at which P_{HG} decreases to 50 %, then the width is about 65 Å, which is in good agreement with previous studies on Alq_3 devices [1,16]. Without DCM2 doping, the host emission zone width can be thinner than 65 Å. Thus the numerical calculation of the exciton distribution with width ~ 20 Å is reasonable when energy transfer may be ignored.

Conclusions

In conclusion, DCM2-doped DPVBi OLEDs were used to study the Förster energy transfer radius R_0 in DPVBi:DCM2 devices. The probability of Förster transfer P_{HG} was found to vary with applied voltage due possibly to trap emission, electric field quenching, and trapped-charge effects. R_0 was estimated to be 30 - 37 Å at low fields. From the energy transfer probability and numerical simulations, the emission zone width was concluded to be ~ 20 Å wide in undoped α-NPD/DPVBi devices.

Acknowledgements

Ames Laboratory is operated by Iowa State University for the U.S. Department of Energy under Contract No. W-7405-Eng-82. This work was supported by the Director for Energy Research, Office of Basic Energy Science.

References

[1] C. W. Tang, S. A. Van Slyke, and C. H. Chen, J. Appl. Phys. **65**, 3610 (1989).

[2] B. W. D'Andrade, M. A. Baldo, C. Adachi, J. Brooks, M. E. Thompson, and S. R. Forrest, Appl. Phys. Lett. **79**, 1045 (2001).

[3] Yuji Hamada, Hiroshi Kanno, Tsuyoshi Tsujioka, Hisakazu Takahashi, and Tatsuro Usuki, Appl. Phys. Lett. **75**, 1682 (1999).

[4] V. Bulović, A. Shoustikov, M. A. Baldo, E. Bose, V.G. Kozlov, M. E. Thompson, and S. R. Forrest, Chem. Phys. Lett. **287**, 455 (1998).

[5] M. Pope and C. E. Swenberg, *Electronic Processes in Organic Crystals* (Oxford University Press, Oxford, 1982).

[6] N. von Malm, J. Steiger, R. Schmechel, and H. von Seggern, J. Appl. Phys. **89**, 5559 (2001).

[7] K. O. Cheon and J. Shinar, Appl. Phys. Lett. **81**, 1738 (2002).

[8] J. Kalinowski, P. Di Marco, V. Fattori, L. Giulietti, and M. Cocchi, J. Appl. Phys. **83**, 4242 (1998).

[9] R. Kersting, U. Lemmer, M. Deussen, H. J. Bakker, R. F. Mahrt, H. Kurz, V. I. Arkhipov, H. Bässler, E. O. Göbel, Phys. Rev. Lett **73**, 1440 (1994).

[10] J. Lam, T. C. Gorjanc, Y. Tao, and M. D'lorio, J. Vac. Sci. Technol. A **18**(2), 593 (2000).

[11] H. Spreitzer, H. Schenk, J. Salbeck, F. Weissoertel, H. Riel, and W. Riess, Proc. SPIE Vol. **3797**, 316 (1999).

[12] R. S. Deshpande, V. Bulović, and S. R. Forrest, Appl. Phys. Lett. **75**, 888 (1999).

[13] W. Brütting, H. Riel, T. Beierlein, and W. Riess, J. Appl. Phys. **89**, 1704 (2001).

[14] J. S. Kim, P. K. H. Ho, N. C. Greenham, and R. H. Friend, J. Appl. Phys. **88**, 1073 (2000).

[15] H. S. Karlsson, K. Read, and R.Haight, J. Vac. Sci. Technol. A **20**(3), 762 (2002).

[16] J. Staudigel, M. Stößel, F. Steuber, and J. Simmerer, J. Appl. Phys. **86**, 3895 (1999).

5. ELECTROLUMINESCENCE SPIKES, TURN-OFF DYNAMICS, AND CHARGE TRAPS IN ORGANIC LIGHT-EMITTING DEVICES

K. O. Cheon and J. Shinar

A manuscript prepared for submission to Physical Review Letters

Abstract

The strong electroluminescence (EL) spike and long decay tail occurring at the turn-off of a bias pulse in some small molecular organic light-emitting devices (OLEDs) are described and analyzed. The observed behavior of the spike is found to be in excellent agreement with a model based on correlated charge pairs, with an average charge pair separation of 20 - 50 Å. Immediately following the spike, a long $1/t$ decay tail is observed. It is formed from the recombination of initially independent charges. It is found that the decay dynamics of the EL spike and tail are strongly dependent on the dynamics of trapped charges in the recombination zone.

Introduction

Organic thin film electroluminescence (EL) has been studied extensively since its demonstration in tris(8-hydroxy quinoline) Al (Alq_3) [1] and poly(*p*-phenylene vinylene) (PPV) [2]. Transient EL has been attracting considerable interest for illuminating basic processes in organic light-emitting devices (OLEDs) [3-6] and for applications requiring pulsed sources. In particular, the turn-off dynamics following a bias pulse have been studied

not only to elucidate the carrier dynamics [4] but also to explore the recombination mechanisms responsible for EL overshoots or spikes [3,7] and long EL decay tails following them, which are observed in several important devices [4,5].

In amorphous organic solids the transport properties are strongly affected by traps, which are generated by energetic disorder, structural disorder, and impurities. These traps reduce the number of mobile carriers and detain charges for a long time; that is, the traps are filled and become charge storage sites. Hence, relatively long-lived trapped charges could exist after the external field is turned off. Relatively long EL decay tails following turn-off should consequently be governed by detrapping processes of these trapped charges [7].

Theory

When a bias is applied to a device, the independent carriers are injected from their electrodes and drift to the recombination zone. The injected carriers can (1) form excitons and (2) correlated charge pairs (CCPs) for light emission, or (3) remain as independent charges. Immediately following the bias turn-off at $t = 0$, all of these three different species exist in the recombination zone. Thus, the emission following turn-off is due to (*i*) decay of (singlet) excitons generated at $t \leq 0$, (*ii*) recombination of CCPs, and (*iii*) recombination of initially ($t = 0$) independent holes and electrons.

(*i*) The decay of the preexisting (singlet) excitons is exponential if their dynamics are governed by monomolecular processes.

(*ii*) The main mechanism of CCP decay [7,8] is closely related to random walk diffusion under the mutual Coulomb interaction [8]. Let $W(r_0, t)$ be the probability that the CCP, with

separation r_0 at $t = 0$, will remain separate at time t. Then their recombination rate $R_{ccp}(t) = -dW/dt$ for a Gaussian-like distribution of separations $g(r_0)$ is given [8] by

$$R_{ccp}(t) = \frac{\sqrt{4\pi}}{\sqrt{D_{ccp}}} \frac{r_c}{t^{3/2}} \int_0^\infty r_0^2 g(r_0) \exp(-\frac{r_0^2}{4D_{ccp}t}) \exp\{-\frac{r_c}{r_0}[1 - erf(\frac{r_0}{\sqrt{4D_{ccp}t}})]\} dr_0 \qquad (1)$$

where D_{ccp} is the CCP diffusion coefficient, $r_c = e^2/(4\pi\varepsilon kT)$ is the Onsager radius ($r_c \sim 17nm$ at room temperature), and *erf* is the error function. The CCP characteristic time for recombination is defined by

$$\tau_{ccp} \equiv \bar{r}^2 / 4D_{ccp}, \qquad (2)$$

where $\bar{r}$ is the median separation. The recombination $R_{ccp}(t)$ has a peak at $t = \tau_{peak}$; the peak is due primarily to the maximum value of $g(r_0)$ at $r_0 = \bar{r}$. Note that $\tau_{peak} \neq \tau_{ccp}$, but rather $\tau_{ccp} \sim 2\tau_{peak}$. At $t \sim \tau_{ccp}$, $R_{ccp}(t)$ is roughly proportional to t^{-2}, but this dependence evolves to $t^{-3/2}$ for $t >> \tau_{ccp}$.

(*iii*) At $t = 0$ there is also a population of independent or uncorrelated charges. They can diffuse away from the charge accumulation zone, or pair up with counter charges to form CCPs and/or excitons. Net diffusion obviously occurs only normal to the layers of the device (the x-direction). Let N_h be the number of holes per unit area localized at the center of the thin recombination zone (i.e., at $x = 0$) at time $t = 0$. Then the time dependent number of holes $p(x,t)$ is given by the Gaussian expression [9]

$$p(x,t) = \frac{N_h}{\sqrt{4\pi D_h t}} \exp(-\frac{x^2}{4D_h t}), \qquad (3)$$

where D_h is the hole diffusion coefficient. The distribution of electrons $n(x,t)$, with initial concentration N_e and diffusivity D_e, obviously satisfies the same relation.

The recombination rate $R_{h\text{-}e}(t)$ of the initially independent charges is given by Langevin equation

$$R_{h-e}(t) = \gamma \int_0^{\Delta x_0} p(x,t)n(x,t)dx = \frac{\gamma N_h N_e}{2\sqrt{\pi(D_h + D_e)}} \times \begin{cases} t^{-1/2} & , \text{ if } t << \tau_{h-e} \\ \dfrac{\Delta x_0}{\sqrt{\pi D_{eff}}} t^{-1} & , \text{ if } t >> \tau_{h-e}. \end{cases} \quad (4)$$

where γ is the bimolecular rate constant, Δx_0 is the width of the recombination zone or charge accumulation zone, and $D_{eff} = (1/D_h + 1/D_e)^{-1}$ is the effective diffusion coefficient of the holes and electrons. The characteristic recombination time of these initially independent charges $\tau_{h\text{-}e}$ is defined as $\tau_{h-e} \equiv \Delta x_0^{\,2} / 4D_{eff}$. $R_{h-e}(t)$ is proportional to $t^{-1/2}$ for $t << \tau_{h-e}$, and to t^{-1} for $t >> \tau_{h-e}$. In order to observe the t^{-1} behavior the charges must be localized in a specific region Δx_0 such as the recombination zone of the OLEDs.

Device structures and measurements

To study the effect of traps on the turn-off dynamics, the selective doping method [10] was used to fabricate matrix arrays of efficient OLEDs based on 4,4'-bis(2,2'-diphenylvinyl)-1,1'-biphenyl (DPVBi) which is one of the most promising blue emitters. The fabrication procedure is described elsewhere [11]; each pixel in the array was ~1.5 mm in diameter. In addition, a 1 nm-thick layer of DPVBi located between the 40 nm-thick undoped 4,4'-bis[N-91-naphthyl)-N-phenyl-amino]biphenyl (α-NPD) hole-transporting layer and the 40 nm-thick neat DPVBi layer was doped with [2-methyl-6-[2-(2,3,6,7-tetrahydro-1H,5H-

benzo[i,j]quinolizin -9-yl)ethenyl]-4H-pyran-4-ylidene]propane-dinitrile (DCM2) (see the inset in Fig. 1). The nominal doping concentrations were 0, 1, 5, and 10 wt.%; the samples were labeled S0, S1, S5, and S10, respectively. In order to improve hole injection, a 5 nm-thick copper phthalocyanine (CuPc) layer was deposited between the indium tin oxide (ITO) anode and the α-NPD layer. Similarly, to enhance electron injection, a 10 nm-thick Alq_3 layer and a 1 nm-thick CsF layer were deposited between the neat layer DPVBi and the 150 nm-thick Al cathode. The overall *RC*-time constant of the sample was estimated to be ~25 ns. Bias pulses with rise- and fall-times of 10 ns were generated using an Avtech Model AV-1011; the EL was monitored using a photomultiplier tube (PMT) with a 50 Ω external load resistance.

Experimental results and discussions

Figure 1 shows that the experimental results are fitted well by the sum of the three terms corresponding to the three mechanisms described above: (*i*) an exponential term due to the prompt exciton decay (dotted line); (*ii*) the term due to CCP recombination $R_{ccp}(t)$, which is responsible for the overshoot (due to the complexity of the graph only the sums of the exponential decay and recombination $R_{ccp}(t)$ are represented by solid lines); (*iii*) the term due to $R_{h\text{-}e}(t)$ (dashed lines), which yields the long emission tail following the overshoot.

(*i*) For all concentrations, the exponential decay was set to the same decay time of 35 ns. This value, however, is not the intrinsic singlet exciton decay time, which is < 10 ns for Alq_3 and DPVBi devices [12]. The source of this discrepancy is the *RC* time constant of ~ 25 ns of

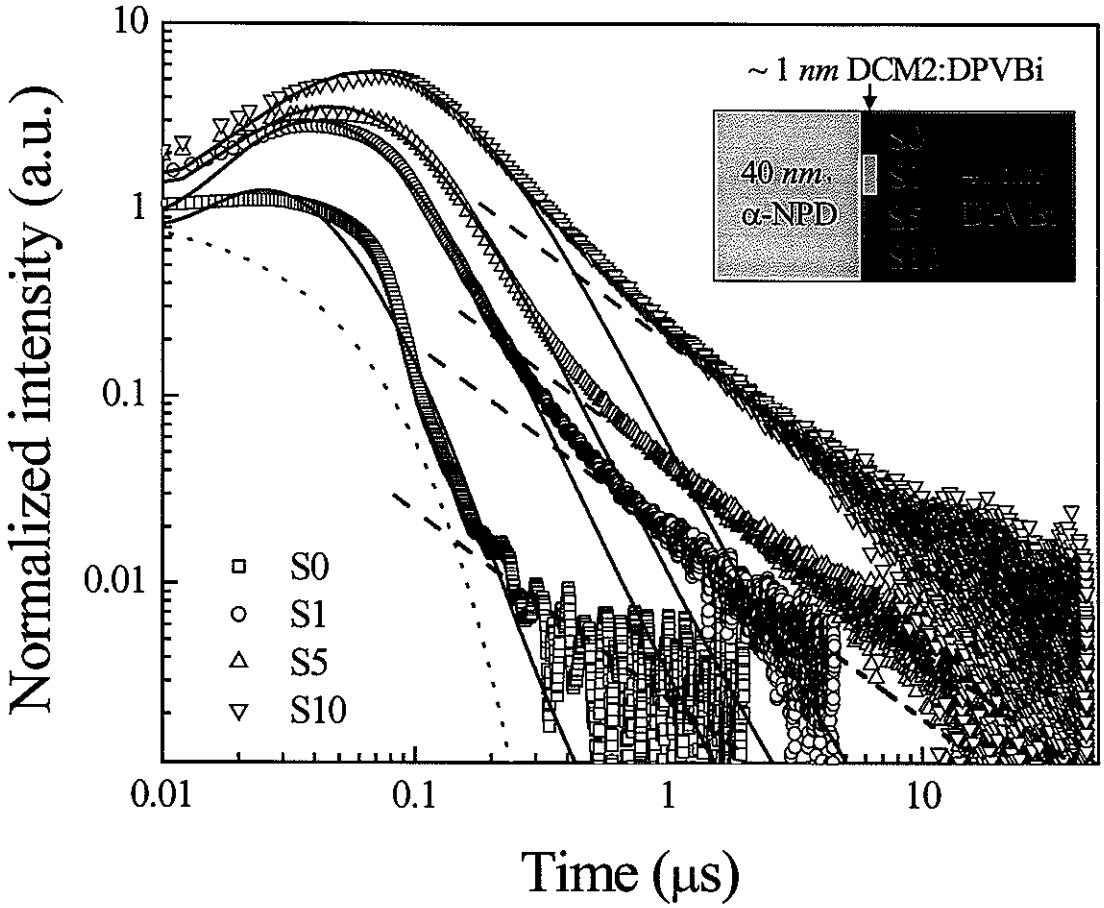

Figure 1. Electroluminescence decay (log-log scale) after external field turn-off in DPVBi OLEDs with different DCM2 doping levels: S0 (0 wt.%), S1 (1 wt.%), S5 (5 wt.%), and S10 (10 wt.%) (see inset). The width of the 12.3 V pulse is 100 μs. The open symbols are the experimental data, the dotted line is the exponential decay of singlet excitons, and the solid lines are the sum of the exponential decay and $R_{ccp}(t)$ (see Eq. (1)). The dashed lines are the predicted emission due to initially independent charges $R_{h\text{-}e}(t)$ see Eq. (4)).

the present devices. This value of *RC*, however, obviously has little effect on the measurements of the longer processes (*ii*) and (*iii*).

(*ii*) The overshoots shown in Fig. 1 increase with increasing DCM2 doping level, even though the doped layer is only 1 nm thick. The overshoot amplitudes, relative to the quasi-steady state EL, are 1.1, 2.8, 3.2, and 5.3 for S0, S1, S5 and S10, respectively. The reason is that the DCM2 molecule, while a fluorophore, is also an electron and hole trapping site (see the energy levels in the inset of Fig. 3). Hence increasing the density of DCM2 traps increases the overshoot amplitude. Indeed, Eq. (1), with $2 \le \bar{r} \le 5$ nm, is in good agreement with the observed overshoots. These values of $\bar{r}$ are close to both the average distance between the DCM2 molecules and the recombination zone width [13]. If we consider the Frenkel exciton localized in a molecule, then CCP separation and charge transfer exciton radii 2 - 5 *nm* are reasonable. Note that $\bar{r} << r_c$ at room temperature. Also note that for a fixed $\bar{r}$ the overshoot width broadens with increased doping concentration; the values of the dispersion parameter $\sigma/\bar{r}$ also increase with doping, due to the increased structural disorder caused by the chemical impurity.

The fit between Eq. (1) and the experimental results yields τ_{ccp} = 0.06, 0.09, 0.12, and 0.15 μs in samples S0 to S10, respectively. This increase in τ_{ccp} is due either to an increasing $\bar{r}$ or a decreasing D_{ccp} (see Eq. (2)). Since $\bar{r}$ should decrease rather than increase at higher doping, we conclude that D_{ccp} decreases due to the deeper DCM2 trap energy (E_t) for higher doping concentration. Indeed, evidence for E_t variation with doping concentration is indirectly provided by the redshift of the dopant emission, which increases with increased doping. This implies that higher doping concentration results in deeper trap-sites. D_{ccp} is

expected to be related to the rate of detrapping from a trap depth E_t, *i.e.*, $D_{ccp} \propto e^{-E_t/kT}$. Thus τ_{ccp} increases with doping concentration.

(*iii*) The dashed lines in Fig. 1 are plots of the initially independent charge recombination $R_{h\text{-}e}(t)$ (Eq. (4)), which are in good agreement with the long $1/t$ tails of EL for all samples. Note that while the $1/t$ dependence is barely observable in the undoped sample S0, it is very clear in the doped samples. However, the $1/\sqrt{t}$ dependence of $R_{h\text{-}e}(t)$ is unobservable, probably masked by the $R_{ccp}(t)$ term.

The $1/t$ tail originates from strong charge accumulation in the recombination zone formed around the internal organic interface. Without doping, the recombination zone width Δx_0 is ~ 5 nm [13], but a 1 nm thick DCM2 doping reduces it to the doped layer thickness. In particular, at more than 1 wt.% doping, a 1 nm thick layer results in almost pure DCM2 emission. Thus the recombination zone is confined to the doped layer.

Figure 2 shows the turn-off dynamics of the EL *vs.* applied bias V_{on} for sample S10. The open squares in the inset are the relative overshoot amplitude; the solid circles are the values of τ_{ccp} determined by fitting $R_{ccp}(t)$ to the experimental results. At low voltage the relative overshoot amplitude increases with V_{on}, reaching a maximum of ~11 at V_{on} ~ 10 V. In contrast, τ_{ccp} decreases monotonically with V_{on}, but it has an inflection point at V_{on} ~ 10 V. Hence it appears that the turn-off dynamics change at ~10 V.

Figure 1 shows that in all the doped samples, the emission following the bias pulse is due mainly to $R_{ccp}(t)$ and $R_{h\text{-}e}(t)$. Hence the area under the emission curve should be proportional to the total number of photons Q_{tot} emitted after the pulse, *i.e.*,

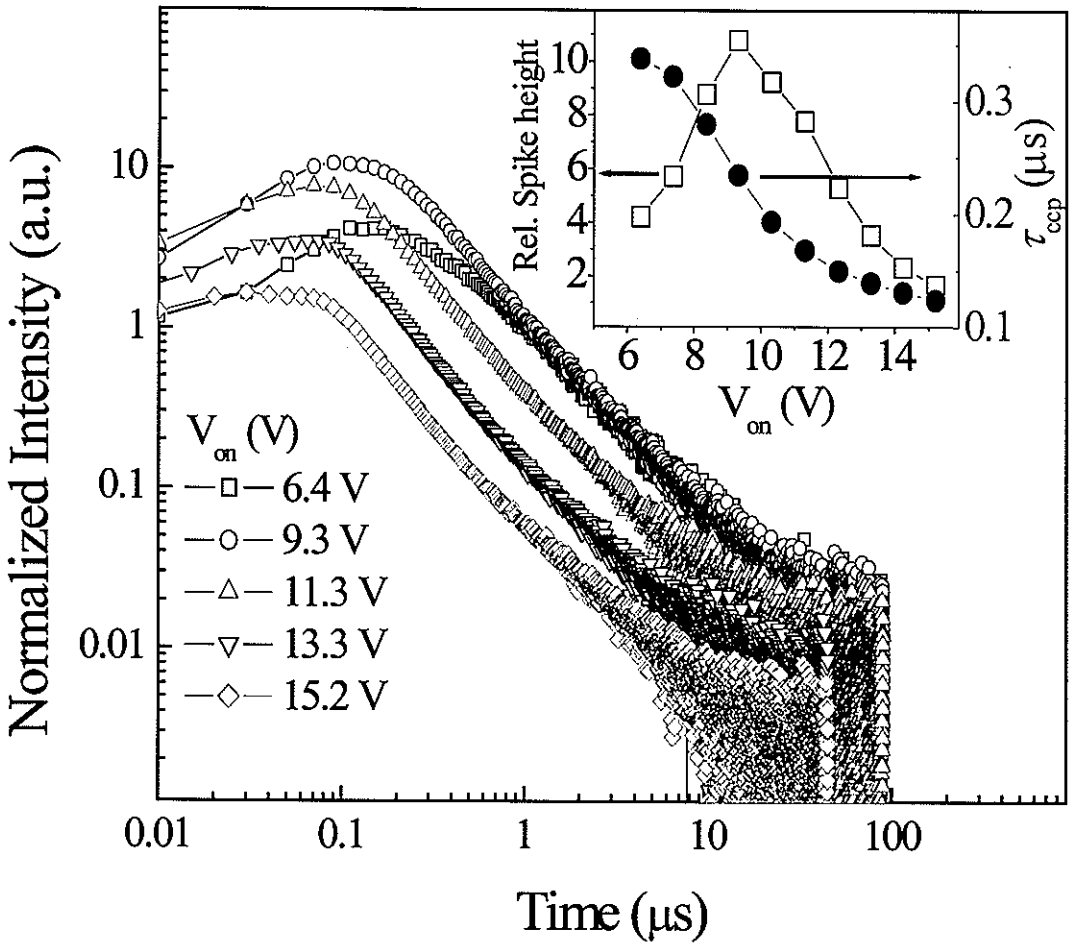

Figure 2. Pulse height V_{on} dependence of the EL spikes and their decay tails in the 10 wt.% doped sample S10; the bias pulse width is 100 μs. The open circles in the inset are the relative overshoot amplitude, normalized to the quasi-steady state EL. The solid circles are the values of τ_{ccp} obtained by fitting Eq. (1) to the observed overshoots.

$$Q_{tot} \propto \int_0^\infty [R_{ccp}(t) + R_{h-e}(t)]dt \,. \tag{5}$$

Although Eq. (5) cannot be solved analytically due to the divergent integrate of $1/t$, but the area can be estimated experimentally. The solid squares in Fig. 3 are the values Q_N of the area under the EL curves, in which the EL intensity at $t = 0$ was normalized to 1. The voltage dependence of Q_N is similar to the voltage dependence of the relative overshoot amplitude (see the inset of Fig. 2). The open circles in Fig. 3 represent the total number of emitted photons Q_{tot}, determined from the steady-state EL level and Q_N.

Q_{tot} is obviously related to the total number of trapped holes P_t and electrons N_t at $t = 0$ in the recombination zone. Specifically, $Q_{tot} < \min\{P_t N_t\}$. Since not all of the recombination events result in EL, the observed Q_{tot} only provides a lower bound for the number of charges trapped on the DCM2 molecules and on intrinsic DPVBi trap-sites. Since in the sample S10 almost all of the emitted photons Q_{tot} come from DCM2 molecules, the total number of possible trap-sites generated by the DCM2 molecules is estimated to be $\sim 3\times10^{11}$ in the 1.5 mm diameter pixel, assuming a simple cubic structure with a 1 nm lattice constant.

The two slopes of Q_{tot} shown are related to the degree of trap filling. The DCM2 molecules in DPVBi are deep traps for holes, but shallower ones for electrons (see the inset of Fig. 3) [14]. Hence, we expect that $P_t > N_t$. Clearly the balance between P_t and N_t is an important factor in determining Q_{tot}. We therefore consider the electron and hole dynamics as a function of the bias.

Due to the barrier for hole hopping from α-NPD to DPVBi (see the inset of Fig. 3), at low voltage only a relatively small fraction of holes are supplied to the doped layer. However, since DCM2 is very deep hole traps in DPVBi, the supplied holes will be trapped

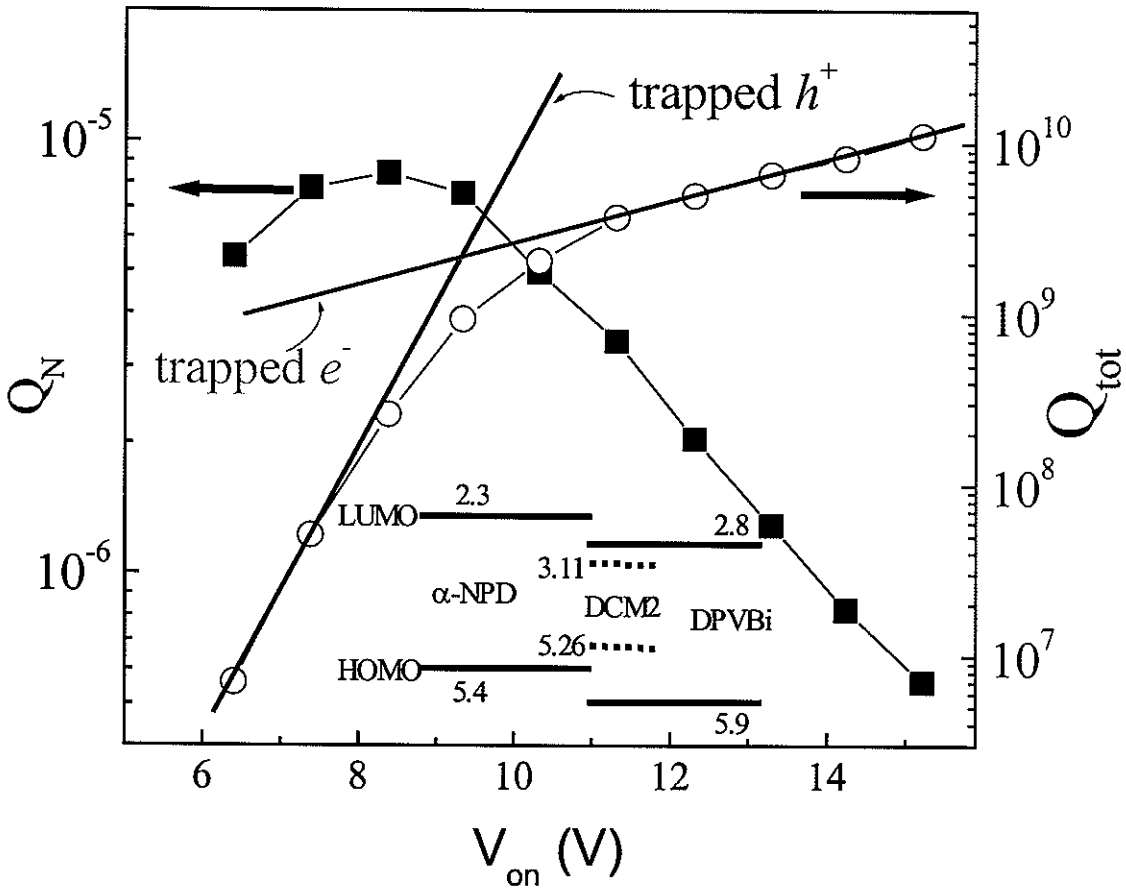

Figure 3. The number of emitted photons after external field turn-off, obtained from under the experimental curves of Fig. 2. Q_N is the area when the quasi-steady state EL is normalized to unity; Q_{tot} is estimated from Q_N and the DC-driven EL. The inset is the schematic energy level diagram [14].

immediately. Hence P_t increases very steeply with increased bias. On the other hand, DCM2 is a relatively shallow trap level for electrons in DPVBi, which is also an electron transport layer. Hence low voltage, more electrons can drift and be trapped in that layer. Thus, with increasing bias, N_t starts from a very high value, and the steep slope of Q_{tot} vs V at low voltage (see Fig. 4) is due to the sharply increasing value of P_t. The lower slope at high voltage is then due to the slowly increasing value of N_t. Hence, it appears that P_t and N_t are well balanced at 9 – 10 V. On this basis, the V_{on}-dependences of the relative overshoot amplitude and τ_{ccp} (see Fig. 3) are due to the degree of trap filling.

Conclusions

In conclusion, the occurrence and behavior of EL spikes or overshoots at the turn-off of voltage pulses in OLEDs containing a narrow DCM2-doped DPVBi recombination zone was described and analyzed. The analysis was based on the behavior of DCM2 as shallow electron and deep hole traps. It showed that the spikes are due to recombination of correlated charge pairs, while the long EL decay tails are due to recombination of initially uncorrelated trapped charges. The total number of photons emitted during the spike provides a lower bound for the density of trapped electrons and holes.

Acknowledgements

Ames Laboratory is operated by Iowa State University for the US Department of Energy under Contract W-7405-Eng-82. This work was supported by the Director for Energy Research, Office of Basic Energy Sciences.

References

[1] C. W. Tang and S. A. VanSlyke, Appl. Phys. Lett. **51**, 913 (1987).

[2] J. H. Burroughes, D. D. C. Bradley, A. R. Brown, R. N. Marks, K. Mackay, R. H. Friend, P. L. Burns, and A. B. Holmes, Nature **347**, 539 (1990).

[3] Y. H. Tak, J. Pommerehne, H. Vestweber, R. Sander, and H. Bässler, Appl. Phys. Lett. **69**, 1291 (1996).

[4] J. Kalinowski, N. Camaioni, P. Di Marco, V. Fattori, and A. Martelli, Appl. Phys. Lett. **72**, 513 (1998).

[5] D. J. Pinner, R. H. Friend, and N. Tessler, Appl. Phys. Lett. **76**, 1137 (2000).

[6] P. W. M. Blom and M. C. J. M. Vissenberg, Phys. Rev. Lett. **80**, 3819 (1998); N. Tessler, N. T. Harrison, and R. H. Friend, Adv. Mater. **10**, 64 (1998); V. G. Kozlov, P. E. Burrows, G. Parthasarathy, and S. R. Forrest, Appl. Phys. Lett. **74**, 1057 (1999); C. I. Wilkinson, D. G. Lidzey, L. C. Palilis, R. B. Fletcher, S. J. Martin, and X. H. Wang, and D. D. C. Bradley, Appl. Phys. Lett. **79**, 171 (2001); J. Wang, R. G. Sun, G. Yu, and A. J. Heeger, J. Appl. Phys. **91**, 2417 (2002).

[7] J. M. Lupton, V. R. Nikitenko, I. D. W. Samuel, and H. Bässler, J. Appl. Phys. **89**, 311 (2001).

[8] A. Mozumder, J. Chem. Phys. **48**, 1659 (1968).

[9] S. M. Sze, *Physics of Semiconductor Devices*, John Wiley & Sons (1981).

[10] J. Lam, T. C. Gorjanc, Y. Tao, and M. D'lorio, J. Vac. Sci. Technol. A **18**(2), 593 (2000).

[11] K. O. Cheon and J. Shinar, Appl. Phys. Lett. **81**, 1783 (2002).

[12] V. Savvateev, J. H. Friedl, L. Zou, J. Shinar, K. Christensen, W. Oldham, L. J. Rothberg, Z. Chen-Esterlit, and R. Kopelman, App. Phys. Lett. **76**, 1501, (2000); T. Nakazawa, M. Asano, S. Fujita, and S. Fujita, Jpn. J. Appl. Phys. **38**, L206 (1999).

[13] C. W. Tang, S. A. VanSlyke, and C. H. Chen, J. Appl. Phys. **65**, 3610 (1989); J. Staudigel, M. Stößel, F. Steuber, and J. Simmerer, J. Appl. Phys. **86**, 3895 (1999); K. O. Cheon, J. Shinar, unpublished results.

[14] M. A. Baldo, C. Adachi, and S. R. Forrest, Phys. Rev. **B 62**, 10967 (2000); C. Hosokawa, H. Higashi, H. Nakamura, and T. Kusumoto, Appl. Phys. Lett. **67**, 3853 (1995); Y. Hamada, H. Kanno, T. Tsujioka, H. Takahashi, and T. Usuki, Appl. Phys. Lett. **75**, 1682 (1999).

6. SUMMARY AND GENERAL CONCLUSIONS

Various aspects of the device physics of doped small molecular OLEDs were described and discussed. The doping layer thickness and concentration were varied systematically to study their effects on device performances, energy transfer, and turn-off dynamics. Low-energy-gap DCM2 guest molecules, in either α-NPD or DPVBi host layers, are optically efficient fluorophores but also generate deep carrier trap-sites. Since their traps reduce the carrier mobility, the current density decreases with increased doping concentration. At the same time, due to efficient energy transfer, the quantum efficiency of the devices is improved by light doping or thin doping thickness, in comparison with the undoped neat devices. However, heavy doping induces concentration quenching effects. Thus, the doping concentration and doping thickness may be optimized for best performance.

Following the introduction to OLEDs given in Chapter 1, very bright multi-color OLEDs including white OLEDs (WOLEDs) were described in Chapter 2. The maximal brightness of the WOLEDs was the highest reported to date. This very high brightness originated from the very efficient undoped DPVBi device itself and highly efficient DCM2 fluorophores: The excitons generated on host DPVBi molecules are efficiently transferred to guest fluorophores; thus, the emission spectra of these guest-host devices are generally composed of two emission bands, that of the host and that of the guest. The intensity ratio of the bands depends on the doping parameters, e.g., doping level. It was also found that the DCM2 doping level affects the peak guest emission wavelength; the peak red-shifts with increasing doping level, which may be due either to the solid state solvation effect (SSSE) or the aggregation of guest molecules. By doping level adjustment, the very bright WOLEDs were

achieved using only two emission bands of the host and the guest, in contrast to inorganic white LEDs, which require three emission bands, typically red, green, and blue.

In order to change the emission color, the doping concentration is typically tuned. However, control of doping concentration is difficult in vacuum-evaporated devices, since the guest and host sources must be adjusted and stabilized. Hence, rather than controlling the color through the doping level, we controlled it through the doped layer thickness (see Chapter 3). Through an one-time adjustment of the doping ratio, the thickness could be continuously varied using a sliding shutter technique. The results described in Chapter 3 showed that as the thickness of the 5 wt.% DCM2-doped layer increased from 0 to 35 Å, the emission color varied continuously from blue to white to red. These doping thickness effects are very similar to the doping level effects on color variation and quantum efficiency. They are explained by a dipole-dipole interaction of the polar DCM2 molecules in a relatively weak polar host medium. Within the dipole-dipole interaction range of ~ 100 Å for DCM2 in α-NPD, the modification of doping thickness and concentration result in similar luminescence behavior due to the interaction between collective dipoles within the range of the dipole of a DCM2 fluorophore.

For the DCM2-doped α-NPD/DPVBi OLEDs, the maximum external quantum efficiency η_{EL}^{ext} = 4.4 % was obtained from very thin (~ 2 Å) DCM2 doped devices; note that for the ideal fluorescent device, where η_{PL} = 100 %, the maximal $\eta_{EL}^{ext} \approx 7 - 8$ %. Therefore, if we consider the solid-state PL quantum yield, where $\eta_{PL} < 100\%$, the observed η_{EL}^{ext} = 4.4 % is about 60 % of the maximal possible efficiency. This implies that the efficiency of the fluorescent devices we fabricated and studied approaches the maximal possible value.

The main mechanism of guest emission in molecular doped system is nonradiative Förster energy transfer from the host to the guest. To date, the values of the Förster energy transfer radius R_0 was estimated from the doping-level dependence of the emission. In Chapter 4, R_0 is determined directly from the probability for energy transfer probability from the main recombination zone to the very thin guest-host layer, since this probability depends on the distance between the main recombination zone and the thin doped layer. The determined value of R_0, which is 30 – 40 Å, is typical of the luminescent organic materials.

From the behavior of OLEDs containing DCM2-doped α-NPD or DPVBi layers, the emission zone is determined from the host-to-guest energy transfer probability. In neat α-NPD/DPVBi OLEDs, most of the light is emitted from the α-NPD/DPVBi interface; the emission zone is ~ 20 Å wide on the DPVBi side. If we insert a very thin DCM2-doped layer in either the α-NPD or the DPVBi layers, then the emission zone swells up to 65 Å due to the energy transfer.

The last chapter of this thesis, Chapter 5, focuses on the turn-off dynamics of DPVBi-band guest-host OLEDs. It is shown that singlet excitons present at $t = 0$, correlated charge pairs, and initially independent holes and electrons all contribute distinctively to the EL decay tail. The preexisting excitons contribute a simple exponential decay tail. However, the relative long-lived emission strongly depends on trap states in the devices. The extrinsic traps are generated by the DCM2 guest molecules. To maximize the trap effects, the DCM2 molecules are doped into the recombination zone of the neat devices. If there is no doping or no intentional traps, then the overshoot signal, which is characteristics of these devices, is relatively weak, as is shown that the overshoot phenomena is due to correlated charge pair recombination. With increased doping concentration, the overshoot amplitudes increases

because more traps generate more correlated charge pairs rather than excitons. From the correlated charge pair model, the pair distance or charge transfer exciton size is estimated to be $\sim 20 - 50$ Å.

Finally, new model is developed to explain the very long decay tail of the EL, which exhibits a $1/t$ behavior. The model, which focuses on the carriers stored in the trap sites, shows that when the external bias is turned off, the trapped holes and electrons diffuse away from the charge accumulation zone. During diffusion, they can "accidentally" recombine to form excitons, via a by Langevin mechanism. Thus, the recombination rate is proportional to $1/t$. These $1/t$-decay tails are the same for all samples; the only difference is their relative amplitude, which increases with increasing DCM2 doping.

ACKNOWLEDGEMENTS

I want to thank Prof. Joseph Shinar who made it possible for me to spend these precious four years in his group. Without his excellent guidance, I could not have performed this research and Ph. D degree. I am deeply indebted to Prof. Paul Canfield, my former adviser, who have kept supporting and encouraging me though I changed my research group.

I would like to thank all my colleges, particularly Moon-Ky Lee for his warm friendship, Chang-Hwan Kim for his useful advices, Dr. Hai-sheng Wu for his kindness discussion, Gang Li, Lijuan Zou, Bhaskar Choudhury, and Zhaoqun Zhou for their help and discussion.

A special thanks and love to my wife, Myungsoon Kim, for her invaluable help in many aspect of my research and family. Without her continuous pointing to the goal probably this work would never have seen happy end. I always feel pleased with my son, Daniel Cheon. He makes me happy and cheerful all the time. I would appreciate my mother for her generous encouragement.

I also appreciate all my seniors and friends in Ames, Dr. Seong-Jae Lee, Dr. Zeehoon Jang, Dr. Changyong Song, Joong-Mok Park, Yungok Ihm, Jong-Ik Park, Yongbin Lee, Sangwook Wu, Yongsung Kim, Jong-Woo Kim, Dr. Ian Fisher, and Dr. Chungyeol Shin. They always advise me in right direction of my life and research.

This work was performed at Ames Laboratory under Contract No. W-7405-Eng-82 with the U.S. Department of Energy. The United States government has assigned the DOE Report number IS-T 2031 to this thesis.